Geoscience Frontiers 13 (2022) 101322

Contents lists available at ScienceDirect

Geoscience Frontiers

journal homepage: www.elsevier.com/locate/gsf

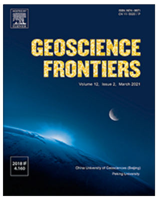

Research Paper

Evolution of $nC_{16}H_{34}$-water–mineral systems in thermal capsules and geological implications for deeply-buried hydrocarbon reservoirs

Guang-Hui Yuan[a,b,*], Zi-Hao Jin[a], Ying-Chang Cao[a,b], Ke-Yu Liu[a], Jon Gluyas[c], Yan-Zhong Wang[a], Ke-Lai Xi[a]

[a] Key Laboratory of Deep Oil and Gas, School of Geosciences, China University of Petroleum, Qingdao 266580, China
[b] Laboratory for Marine Mineral Resources, Qingdao National Laboratory for Marine Science and Technology, No. 62, Fuzhou South Road, Qingdao 266071, China
[c] Department of Earth Sciences, Durham University, Durham DH1 3LE, UK

ARTICLE INFO

Article history:
Received 4 May 2021
Revised 30 September 2021
Accepted 23 October 2021
Available online 27 October 2021
Handling Editor: V.O. Samuel

Keywords:
$nC_{16}H_{34}$-water–mineral systems
Organic-inorganic interactions
Hydrocarbon degradation
Mineral alteration
Deeply buried hot reservoirs

ABSTRACT

Organic-inorganic interactions between hydrocarbons and most minerals in deeply buried reservoirs remain unclear. In this study, gold capsules and fused silica capillary capsules (FSCCs) with different combinations of $nC_{16}H_{34}$, water (distilled water, $CaCl_2$ water) and minerals (quartz, feldspar, calcite, kaolinite, smectite, and illite) were heated at 340 °C for 3–10 d, to investigate the evolution and reaction pathways of the organic–inorganic interactions in different hot systems.

After heating, minerals exhibited little alteration in the anhydrous systems. Mineral alterations, however, occurred obviously in the hydrous systems. Different inorganic components affected $nC_{16}H_{34}$ degradation differently. Overall, water promoted the free-radical thermal-cracking reaction and step oxidation reaction but suppressed the free-radical cross-linking reaction. The impact of $CaCl_2$ water on the $nC_{16}H_{34}$ degradation was weaker than the distilled water as high Ca^{2+} concentration suppressed the formation of free radicals. The presence of different waters also affects the impact of different minerals on $nC_{16}H_{34}$ degradation, via its impact on mineral alterations. In the anhydrous $nC_{16}H_{34}$-mineral systems, calcite and clays catalyzed generation of low-molecular-weight (LMW) alkanes, particularly the clays. Quartz, feldspar, and calcite catalyzed generation of high-molecular-weight (HMW) alkanes and PAHs, whereas clays catalyzed the generation of LMW alkanes and mono-bicyclic aromatic hydrocarbons (M-BAHs). In the hydrous $nC_{16}H_{34}$-distilled water–mineral systems, all minerals but quartz promoted $nC_{16}H_{34}$ degradation to generate more LMW alkanes, less HMW alkanes and PAHs. In the $nC_{16}H_{34}$-$CaCl_2$ water–mineral systems, the promotion impact of minerals was weaker than that in the systems with distilled water.

This study demonstrated the generation of different hydrocarbons with different fluorescence colors in the different $nC_{16}H_{34}$-water–mineral systems after heating for the same time, implying that fluorescence colors need to be interpreted carefully in investigation of hydrocarbon charging histories and oil origins in deeply buried reservoirs. Besides, the organic–inorganic interactions in different $nC_{16}H_{34}$-water–mineral systems proceeded in different pathways at different rates, which likely led to preservation of liquid hydrocarbons at different depth (temperature). Thus, quantitative investigations of the reaction kinetics in different hydrocarbon-water-rock systems are required to improve the prediction of hydrocarbon evolution in deeply buried hydrocarbon reservoirs.

1. Introduction

After hydrocarbon charging, water is still ubiquitous in most deeply-buried reservoirs with various mineral compositions (Siskin and Katritzky, 1991; Helgeson et al., 1993; Girard et al., 2002; Zou et al., 2013; Zhao et al., 2018; Yuan et al., 2019a). Since formation temperature and pressure increase following deep burial processes after oil charging, organic–inorganic interactions among hydrocarbons, water and minerals are ubiquitous, and play an important role in oil stability (Surdam and Crossey, 1987; Helgeson et al., 1993; Price, 1993; Worden et al., 1998, 2017; Seewald, 2001, 2003; Molenaar et al., 2008; Zhang et al., 2008a, b; van Berk et al., 2013; Liu et al., 2019; Yuan et al., 2019b; Pang et al., 2020; Xu et al, 2021) and quality evolution of both the hydrocarbons and the reservoirs (Worden et al., 1998, 2017; Higgs et al.,

---

* Corresponding author.
E-mail address: yuan.guanghui@upc.edu.cn (G.-H. Yuan).

https://doi.org/10.1016/j.gsf.2021.101322

2007; van Berk et al., 2013; Lai et al., 2017; Yuan et al., 2018; Yuan et al., 2019b). Over the past half century, significant advances have been achieved on our understanding of the respective reaction pathways of oil generation and degradation, and rock diagenesis in petroliferous basins (Surdam and Crossey, 1987; Lewan, 1997; Seewald, 2003; Tian et al., 2006; Pan et al., 2010; Molenaar et al., 2015; Yuan et al., 2019a,b). The impact of some inorganic compositions (eg. water, minerals, rare elements) on degradation of kerogen, oil, and organic acids have also been investigated extensively (Hoering, 1984; Eglinton et al., 1986; Siskin and Katritzky, 1991; Lewan, 1997; Pan et al., 2009, 2010; Wei et al., 2019; Xu et al., 2020; Wan et al., 2021). The coupling evolution processes and coupling mechanisms of the relevant organic and inorganic reactions in deeply buried hot systems with complex geofluids and mineral compositions, however, still need further investigation (Yuan et al., 2019b; Wan et al., 2021).

In subsurface reservoirs, rocks generally contain different minerals including feldspar, quartz, calcite, kaolinite, illite and sometimes smectite and chlorite (Glasmann, 1992; Higgs et al., 2007, 2013; Bjørlykke, 2014; Macquaker et al., 2014; Yuan et al., 2015; Mu et al., 2016). The experiment results of previous study on thermal oil–water-feldspar systems showed that feldspar minerals and crude oil have significant mutual influence on each other's evolution in the presence of water at elevated temperatures (Yuan et al., 2019b). To date, however, the details of the mutual interactions between hydrocarbons and other different minerals but the feldspar, and the genesis of the interactions in deeply buried hot hydrocarbon reservoirs are still unclear. Some thermal experiments analyzed the impact of water or minerals (rocks) on degradation of organic matters including alkanes, crude oil and organic acids (Seewald, 2001, 2003; Zhao et al., 2007; Pan et al., 2009, 2010; Bu et al., 2017; Wei et al., 2019). For example, Seewald (2001, 2003) analyzed the impact of iron mineral on decomposition of low-molecular-weight (LMW) hydrocarbons in hot hydrocarbon-water-iron mineral systems with a high water/hydrocarbon ratio and proposed the stepwise oxidation mechanism. Zhao et al (2007) analyzed the effect of rocks of sandstone, mudstone and carbonate on gas formation during oil degradation using thermal experiments in gold capsules. Other studies analyzed the impact of individual minerals, such as calcite and smectite (Pan et al., 2010), as well as illite, smectite, quartz, and calcite (Xiao et al., 2010), on oil degradation using thermal experiments in gold capsules. These studies, however, focused mainly on the gas generation yields but did not investigate the detailed evolution of liquid hydrocarbons, water and minerals, making it impossible to decipher the coupled organic and inorganic interactions (Yuan et al., 2019b). Hence, studies based on the coupled evolution of various minerals and hydrocarbons in different thermal hydrocarbon-water-mineral systems are warranted.

Thermal simulation in high-temperature and high-pressure (HTHP) reactors is an important method to investigate the detailed evolution processes of organic–inorganic interactions between geofluids and rocks in subsurface reservoirs (Lewan, 1997; Waples, 2000; Seewald, 2001; Zhang et al., 2008b; Fu et al., 2009; Tian et al., 2010; Bu et al., 2017). HTHP Hastelloy reactors and gold capsule reactors have been widely used to conduct thermal experiments including pyrolysis experiments (Lewan, 1997; Waples, 2000; Seewald, 2001; Hill et al., 2003; Tian et al., 2006; Zhao et al., 2007; Zhang et al., 2008a, b; Yuan et al., 2019b) and water–rock experiments (Fu et al., 2009; Zhu and Lu, 2009; Tutolo et al., 2015; Li et al., 2017, 2018) to reproduce various organic–inorganic interactions. The products and remnants in these reactors, however, can be analyzed only after opening of the reactors, and direct observation of the complex interactions occurring in the HTHP systems cannot be performed. Because of the advantage of HTHP resistance, fused silica capillary capsules (FSCCs) have been used to conduct various thermal simulation experiments (Chou et al., 2008; Shang et al., 2009; Ong et al., 2013; Wang et al., 2016; Xu and Chou, 2017). Different from Hastelloy reactors or gold capsules, direct analysis (e.g. laser Raman spectroscopy and fluorescence color and spectrum analysis) can be easily conducted on the newly generated and remnant materials in the transparent FSCCs without breaking the capsules (Bourdet et al., 2014; Caumon et al., 2014; Chou and Wang, 2017; Xu and Chou, 2017; Wang et al., 2018). This allows for the direct and continuous observation of the evolution of the solid, liquid, and gaseous masses in the FSCCs. Some studies have attempted to analyze alkane degradation using FSCCs by conducting an analysis of the gases and water solutions using laser Raman spectroscopy (Chou et al., 2008; Xu and Chou, 2017; Wang et al., 2018). Liquid hydrocarbons, however, were not analyzed due to the influence of the fluorescence on the Raman signals.

In this study, both gold capsules and FSCCs were used to conduct thermal experiments to investigate the evolution and decipher the genesis of the organic–inorganic interactions in hot $nC_{16}H_{34}$-water–mineral systems. Three series of thermal experiments were conducted at 340 °C with various combinations of reactants including $nC_{16}H_{34}$, water (distilled (D) water, $CaCl_2$ water), and minerals (feldspar, quartz, calcite, kaolinite, smectite, and illite) (Supplementary data, Tables S1, S2). The first anhydrous series of experiments were conducted without water, the second hydrous series with D water, and the third hydrous series with $CaCl_2$ water. The experiments in the gold capsules were conducted for 10 d to obtain quantitative data, and the experiments in the FSCCs were conducted for three different periods of 3, 6 and 10 d, respectively, to observe detailed evolution of the interactions. The kinetics of oil degradation (Waples, 2000) and mineral alteration (Palandri and Kharaka, 2004) suggest that heating experiments at 340 °C for 3, 6, and 10 d may produce results similar to subsurface hydrocarbon reservoirs heated at 160 °C for approximately 2000, 4000 and 7000 yr, respectively. In addition, a temperature of 340 °C is lower than the critical temperature of water (374 °C for deionized water and higher for saline water) (Haas, 1976; Lewan, 1997), and supercritical water is avoided in the present experiments. For the first time, the continuous evolution of gases, liquid hydrocarbons, and other organics dissolved in water in different $nC_{16}H_{34}$-water–mineral systems was investigated using laser Raman spectroscopy, fluorescence color and fluorescence spectrum analysis, and gas chromatography (GC). In addition, the textural and mineral evolution of the minerals was identified using scanning electron microscopy (SEM) with an energy dispersive spectrometer (EDS) after opening the FSCCs. The objectives of this study are to (i) describe the evolution of alkanes and minerals in different $nC_{16}H_{34}$-water–mineral systems; (ii) investigate the impact of water and minerals on alkane degradation; (iii) investigate the possible pathways of organic–inorganic interactions in different geochemical systems; (iv) propose geological implications for organic–inorganic interactions in deeply buried hydrocarbon reservoirs.

2. Samples and analytical methods

2.1. Sample preparation

Crude oils generally contain a large number of alkanes, aromatics, reins, asphaltenes and even organic acids. At elevated temperature, any individual alkane generates a large number of various light and heavy products (Kissin, 1996), thus heating of a crude oil would produce extremely complex pyrolysis products that may originating from different components of the crude oil, which may shadow elucidation of hydrocarbon degradation mechanisms.

In order to make the experimental results to reflect the evolution processes directly, pure $nC_{16}H_{34}$ (>99.5%), an important composition in mature crude oil was employed in this study. With a melting point of 18.2 °C, the liquid state of the $nC_{16}H_{34}$ at room temperature promise easy loading of the sample in the FSCCs. A $CaCl_2$ solution with a concentration of 25 g/L was prepared with 99.99% $CaCl_2$ and distilled water (D water) (>18.21 MΩ·cm @ 25 °C).

Six types of minerals (quartz, K-feldspar, calcite, smectite, kaolinite, and illite) that serve as main compositions in subsurface rocks were used in this study. K-feldspar but albite was used because dissolution of K-feldspar is commonly ubiquitous in the deeply buried reservoirs; albite, however, generally exist in the form of grains or albite cements. Chlorite was not used in the present study because it generally experienced little chemical alteration during the deep burial processes. Quartz, feldspar and calcite were ground and sieved to retain a size fraction between 200 mesh (75 μm) and 240 mesh (60 μm). The minerals were ultrasonically cleaned three times with dichloromethane and D water to remove the attached impurities and organic matter. The minerals were then dried at 60 °C and analyzed with an X-ray diffractometer (Supplementary Table S3). No organic materials were detected in the mineral samples. The quartz, feldspar (K-feldspar), calcite, and illite used in this study were of high purity (>99%), and the purity of the smectite and kaolinite was higher than 90%; some minor quartz grains that could not be separated were dominant in the 10% impurity.

2.2. Thermal simulation experiments

2.2.1. Gold capsule preparation and heating

Gold capsules (each 6 cm long) were prepared using pure gold with an OD of 6 mm and wall thickness of 0.25 mm. The gold capsules were welded at one end before loading samples. Then, three series of samples of $nC_{16}H_{34}$ plus minerals, $nC_{16}H_{34}$-D water plus minerals, and $nC_{16}H_{34}$-$CaCl_2$ water plus minerals were loaded into the gold capsules. $nC_{16}H_{34}$ was loaded firstly, followed by water and lastly minerals, which avoiding possible sealing of air in the mixtures. The amounts of $nC_{16}H_{34}$, water, and minerals were approximately 50, 100, and 100 mg, respectively (Supplementary data, Table S1). After loading, the welded end of the gold capsules was submerged in cold water and the open end of each capsule was purged with argon to remove air in the gold capsules, then the open end was welded in the presence of argon.

The experimental heating system has room for seven pressure vessels in one furnace. A fan installed at the bottom of the furnace ensures the same time for all vessels inside the furnace. Three gold capsules containing $nC_{16}H_{34}$, $nC_{16}H_{34}$-D water plus minerals, and $nC_{16}H_{34}$-$CaCl_2$ water plus minerals, respectively, were placed into one of the seven single vessels. The vessels were connected with pipelines, and the internal pressure was maintained at 50 ± 0.1 M Pa by pumping water into or out of the vessels, which prevent leakage of the gold capsules due to an increase om the internal pressure during the heating process. The vessels were heated in the oven at 340 ± 1 °C, identical to the FSCC experiments. The vessels with gold capsules were removed from the oven after heating for 10 d, and were quenched to room temperature in cold water within 10 min. After dying, the gold capsules were weighted to check weight difference before and after heating to make sure no leakage of the capsules during the experiments.

2.2.2. FSCC preparation and heating

The FSCCs (each 8 cm long) were prepared using silica capillary tubes produced by Polymicro Technologies, with an outer diameter (OD) of 794 ± 12 μm and an inner diameter (ID) of 400 ± 3 μm.

The FSCCs were firstly burned in a hydrogen flame to remove the polyimide coating layer, and then were washed with dichloromethane and D water to remove the burnt residue. After cleaning and drying, the liquid samples ($nC_{16}H_{34}$, water) were suctioned into one end of the FSCCs by capillary force; then, the other end of the tubes were sealed using the hydrogen flame. The FSCCs were then centrifuged at 3000 rpm to move the liquid samples to the sealed ends. Subsequently, the grains of different minerals were loaded into the FSCCs through the open end by airflow using a pipette; the mineral weights in the FSCCs were then obtained by determining the weight difference before and after loading the minerals using an AS 60/220. R2 Analytical Balance (error ± 0.06 mg). Overall, approximately 4 ± 0.5 mm of the $nC_{16}H_{34}$ and water and 3 ± 0.5 mg of minerals were filled in the FSCCs (Supplementary data, Table S2). After filling of samples, the sealed end of the FSCCs were quickly merged into ice-water. The open end of the tubes was then connected to a vacuum pumping & N_2 filling system (Supplementary data, Fig. S1), the air was removed and N_2 was filled in the FSCCs. Lastly, the open end of the tubes was sealed rapidly under the protection of nitrogen to avoid entering of air in the FSCCs.

For safety reasons, the FSCCs were placed in one-end sealed copper tubes of about 4 mm in diameter. The copper tubes with the FSCCs were loaded in a muffle furnace that contained a single thermocouple to record the temperature. The FSCCs were heated in the oven at 340 ± 2 °C for 3 d for the first period, 6 d for the second period, and 10 d for the third period. At the end of each heating period, the FSCCs were removed from the oven to cool to room temperature in the air. Lastly, the FSCCs were removed from the copper tubes for a detailed analysis of the generated and remnant gases, liquids, and solids.

2.3. Analysis of gases, liquids, and minerals

2.3.1. Analytical methods for the gases and liquids in gold capsules

After heating, the gaseous components in the gold capsules were collected in a special device connected to an Agilent 6890 N GC modified by Wasson ECE Instrumentation. After the capsule was placed into the device, the whole device was evacuated to $<1 \times 10^{-2}$ Pa. The gold capsule was then pierced in the vacuum device with a needle, allowing the gases to escape into the device. The valve connecting the device and the modified gas chromatograph remained open for a short period to allow the gas fully escape into the GC. In this manner, the GC analyses of the organic and inorganic gas components were performed using an automatically controlled procedure. The oven temperature for the gaseous hydrocarbons analysis was initially held at 70 °C for 6 min, ramped from 70 °C to 130 °C at 15 °C/min, from 130 °C to 180 °C at 25 °C/min, and was then held at 180 °C for 4 min. For the inorganic gas analysis, the temperature was held at 90 °C.

After the GC analysis of the gas components, the light hydrocarbons in each gold capsule were first collected in a vial with 3 mL pentane by liquid nitrogen freezing; the gold capsule was then placed into the vial quickly to collect the liquid hydrocarbon components left inside of the capsule. With liquid nitrogen freezing, an internal deuterated nC_{24} standard of 3.40 mg was added to each vial, and the vials were sealed as soon as possible. Following ultrasonic treatments of 5 min, the vials were allowed to settle for 72 h until the pentane solutions became clear. The pentane solutions (total pentane extracts) in all the vials were directly injected into the HP6890 gas chromatograph fitted with a 30 mm × 0.32 mm i.d. column coated with a 0.25-mm film of HP-5, employing nitrogen as a carrier gas. The oven temperature was programmed as follows: 50 °C for 5 min, raised from 50 °C to 150 °C at 2 °C/min, and from 150 °C to 290 °C at 4 °C/min, and then held at 290 °C for 15 min.

2.3.2. Analytical methods for the gases, liquids, and minerals in the FSCCs

Following heating, the FSCCs were loaded into a centrifuge (at 4000 rpm) protected by degreased cotton to separate the coexisting phases and concentrate the gases, water, and the liquid hydrocarbons. After centrifugation, gas, water and liquid hydrocarbons were distinguished with using an Axioskop 40 microscope (Carl Zeiss) with a UV light. The gases and waters in the FSCCs were analyzed using a Renishaw inVia Raman microscope with matching UV light to obtain the Raman spectra of the different phases. The Renishaw inVia Raman microscope was used to acquire the spectra using 514 nm laser excitation, a 20 × Olympus objective with 0.25 numerical aperture, and a 600-groove/mm grating with a spectral resolution of about 2 cm^{-1}; a ~18 mW laser light was focused on the sample during the measurement. The accumulation time was 30 s for each step, and 3 accumulations were conducted for every spectrum. The Raman signals from 100 cm^{-1} to 4400 cm^{-1} were collected to determine the spectral features of each phase and identify its composition. With the same initial N_2 pressure of 1 bar in the sealed FSCCs, the absolute concentration of N_2 in each FSCC before and after heating should be identical. Thus, comparison of the Raman signal intensity between the generated gases (gaseous hydrocarbons, CO_2) and the N_2 can be used to assess the relative yields of the gases in the FSCCs (Chou and Wang, 2017). To do this, the fluorescence background was subtracted and the Raman spectra was multiplied by a constant to obtain the same peak height of N_2.

Fluorescence refers to the emission of photons from specific bonds in molecules during the excitation by UV light. When applied to hydrocarbons, the molecules are aromatics, resins, and asphaltenes, while saturates do not fluoresce (Bourdet et al., 2012, 2014). The signatures of the fluorescence spectra of the liquid hydrocarbons, however, can still be correlated with the *n*-alkane profiles of the hydrocarbons, and a shift of spectra λ_{max} (wavelength of the maximum intensity) to longer wavelength generally indicates larger *n*-alkane numbers (Liu et al., 2014). Due to the strong influence of fluorescence (Wang et al., 2018), satisfactory Raman spectra of the liquid hydrocarbons in the FSCCs were not obtained in this study, even laser excitations from 256 nm to 1064 nm was tried. In order to obtain detailed chemical information and overcome human bias in color perception, fluorescence spectrometry was also performed on the liquid hydrocarbons after identification of the fluorescence color. The liquid hydrocarbons in the FSCCs were detected using a Leica SP5 laser scanning confocal microscope with a 405 nm laser and a detection range of 400–800 nm with a step size of 10 nm. After collection of the normalized fluorescence spectra, the values of λ_{max} (wavelength of the maximum intensity), parameters including $Q_{650/500}$ (ratio of the intensity at 650 nm to the intensity at 500 nm) and QF_{535} (ratio of the 535–750 nm flux to the 430–535 nm flux) that can be used to indicate blue/red shift of the spectra were calculated (Stasiuk and Snowdon, 1997; Bourdet et al., 2012, 2014; Liu et al., 2014; Cheng et al., 2019; Ping et al., 2019). In conjunction with the fluorescence color, these data provide information on the evolution of the liquid hydrocarbons.

After analysis of the gases, waters, and liquid hydrocarbons, the FSCCs were placed into liquid nitrogen to freeze the generated gases and decrease the internal pressure in the FSCCs; subsequently, each FSCC was cut to open and the minerals in the tubes were removed with a dropper. After removing the alkane adhering to the mineral surfaces using dichloromethane and D water, the minerals were dried and fixed on aluminum stubs with conducting tape and were coated with gold. The texture and secondary mineralization after reaction were examined using a Coxem-30plus SEM. An EDS system (XFlasher Detector 430-M), which allows for the analysis at a spot of about 1 μm in diameter, was used to test the elemental composition of the minerals, with an error of 0.1%.

3. Results

3.1. Gaseous components

3.1.1. Yield of gases in the gold capsules

The yields of the gases produced in the gold capsules after 10-d heating are presented in Fig. 1 and Supplementary data, Table S4. Overall, the hydrous systems with D water had the highest gas yields, followed by the hydrous systems with $CaCl_2$ water, and lastly the anhydrous systems without water (Fig. 1). C_1-$n$$C_4$ alkanes dominated the gaseous hydrocarbons in all the experiments. Isobutene ($i$$C_4$), isopentane ($i$$C_5$), ethene and propene were generated, but with much lower yields (Supplementary data, Table S4). H_2 was detected in all the gold capsules, but CO_2 was detected only in the hydrous systems (Supplementary data, Table S4).

In the anhydrous systems without minerals (I’-a), ethane (0.25 mL/g) and propane (0.24 mL/g) dominated the gases, followed by methane (0.13 mL/g), butane (0.13 mL/g), hydrogen gas (0.08 mL/g) and pentane (0.02 mL/g) (Fig. 1a; Supplementary data, Table S4). With the addition of quartz (I’-a) and feldspar (I’-b), the yields of the gases show little difference with the I’-a system, particularly the quartz. In contrast, the addition of kaolinite (I’-e), smectite (I’-f) and illite (I’-g) in the gold capsules resulted in much more generation of C_1-$n$$C_4$ gases (0.25–0.64 mL/g) and H_2 (0.31–0.49 mL/g). The presence of calcite (I’-d) also led to generation of more C_1-$n$$C_4$ gases (0.17–0.35 mL/g) and H_2 (0.27 mL/g), but less than the clay minerals. Different from the systems with quartz, feldspar, and calcite, the ratios of $i$$C_4$/$n$$C_4$ increased significantly with the presence of clays (particularly smectite) (Supplementary data, Table S4). Overall, the yield of methane was lower than that of ethane and propane in most anhydrous systems (Fig. 1a; Supplementary data, Table S4).

In the hydrous systems with D water (II’-a), much more C_1-C_4 gases (0.38–0.59 mL/g), H_2 (1.21 mL/g) and CO_2 (0.31 mL/g) (Fig. 1b; Supplementary data, Table S4) were generated than in the I’-a anhydrous system. The presence of quartz in the II’-b system resulted in lower yields of C_1-C_3 gases (0.21–0.44 mL/g), H_2 (0.93 mL/g), and CO_2 (0.09 mL/g), although more butane (1.00 mL/g) was generated. With the addition of feldspar, calcite, and clay minerals, significant increases in the yields of C_1-C_3 gases and CO_2 were recorded, but the yield of H_2 decreased significantly (Fig. 1b). The systems with clays had the highest yields of C_1-C_3 gases, followed by calcite and feldspar. The yield of *n*-butane in the $nC_{16}H_{34}$-D water systems with feldspar (II’-b), calcite (II’-c), and kaolinite (II’-d) were lower than that of the $nC_{16}H_{34}$-D water system without minerals, while the yields of *n*-butane were higher in the experiments with smectite (II’-f) and illite (II’-g). All minerals had little impact on the $i$$C_4$/$n$$C_4$ ratio, but the clays increased the $i$$C_5$/$n$$C_5$ ratios (Supplementary data, Table S4). Different from the anhydrous system, the methane yield was higher than that of ethane and propane in the hydrous systems with D water (Fig. 1a,b; Supplementary data, Table S4).

Comparison of the gas yields in the IIII’-a, I’-a and II’-a systems demonstrate that the $nC_{16}H_{34}$-$CaCl_2$ water system generated less gaseous hydrocarbons, CO_2, and H_2 than the $nC_{16}H_{34}$-D water system, but the yields were higher than those in the anhydrous system (Fig. 1a–c; Supplementary data, Table S4). Quartz decreased the gas yields in the III’-b system, and feldspar had little impact on the gas yields. In contrast, the addition of calcite and clays led to the generation of more C_1-$n$$C_4$ gases and CO_2, particularly in

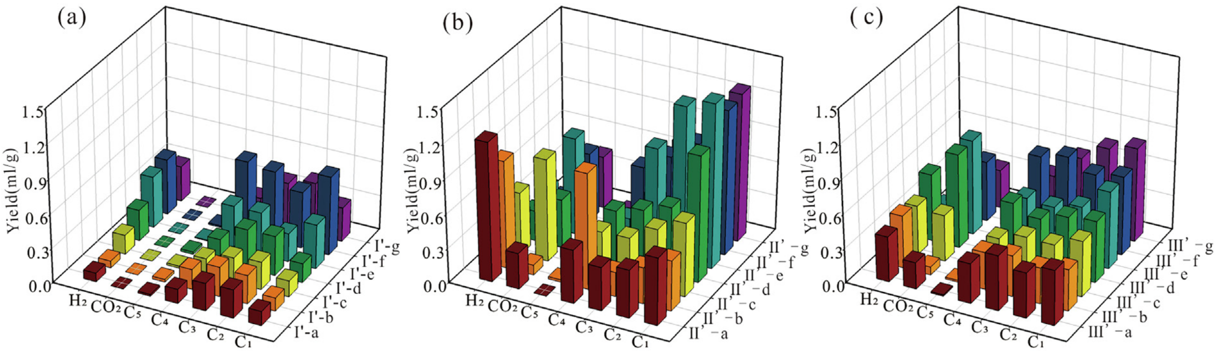

Fig. 1. Yields of the main gases (C_1-nC_5 alkanes, H_2, and CO_2) in different gold capsules after 10-d heating. (a) Anhydrous systems; (b) hydrous system with D-water; (c) hydrous system with $CaCl_2$ water.

the presence of clays (Fig. 1c; Supplementary data, Table S4). The presence of clays slightly increased the iC_4/nC_4 and iC_5/nC_5 ratios (Supplementary data, Table S4). Similar to the systems with D water, the yield of methane was higher than ethane and propane in the hydrous systems with $CaCl_2$ water.

3.1.2. Raman spectra of gaseous hydrocarbons in the FSCCs

In the FSCCs prior to heating, only nitrogen was detected by the Raman spectra (the N═N bending band at 2332 cm^{-1}). After heating, Raman signals of different gaseous hydrocarbons with different intensities were detected in all the FSCCs (Fig. 2; Supplementary data, Fig. S2), and the signals became stronger as the experiments lasted from 3 d to 10 d.

In the anhydrous I-a FSCC with only $nC_{16}H_{34}$, the laser Raman responses of the gaseous hydrocarbons were very weak after 3–6 d heating (Fig. 2a1, a2). Consistent with the gold capsules, the Raman signals of methane (2920 cm^{-1}), ethane (2902 cm^{-1} and 2958 cm^{-1}) (Chou et al., 2008; Chou and Wang, 2017; Xu and Chou, 2017) were clearly visible in the 10-d experiment (Fig. 2a2). Propane (2887 cm^{-1}, 2932 cm^{-1}, 2975 cm^{-1}) and *n*-butane (2889 cm^{-1}, 2948 cm^{-1}) cannot be separated totally using the very close Raman peak of 2887–2889 cm^{-1}, however, they can be distinguished by the 2932 cm^{-1} peak and the 2948 cm^{-1} peak. Besides the *n*-alkanes, *i*-butane (Chou et al., 2008) was identified at the 2878 cm^{-1} peak, but the signal was much weaker than that of C_1-nC_4. In addition to the alkane gases, a weak Raman signal of ethene (3025 cm^{-1}) (Wang et al., 2013; Magnotti et al., 2015), was also identified after 6–10 d heating in this study. The ethane, however, was not detected in the FSCCs of previous studies (Chou et al., 2008; Xu and Chou, 2017; Wang et al., 2018). In the $nC_{16}H_{34}$-mineral systems with feldspar (I-c), calcite (I-d), kaolinite (I-e), smectite (I-f), and illite (I-g), the Raman peaks of C_1-C_3 alkanes and ethene were evident after 6-d heating (Fig. 2c–g). Higher concentrations of the C_1-C_3 gases were gener-

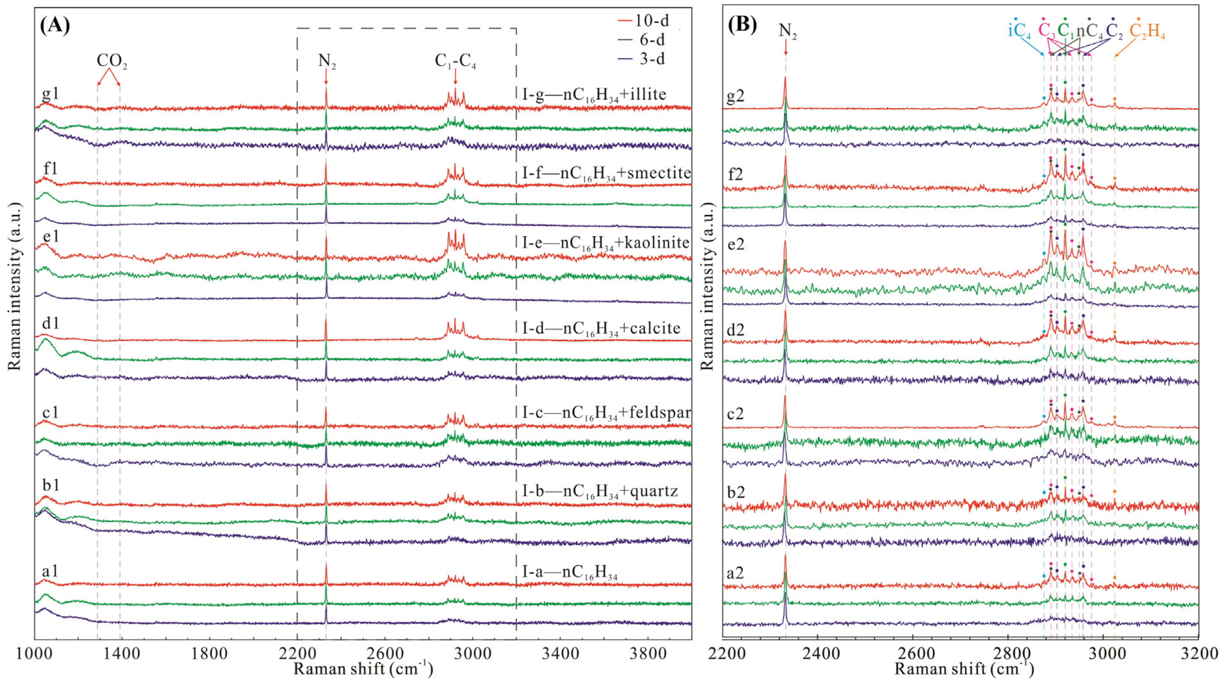

Fig. 2. (A) Laser Raman spectra of the vapor phases in the anhydrous experiments after 3-d, 6-d and 10-d heating. (B) Enlargement of the Raman signals of the gaseous hydrocarbons. The presence of CH_4 is indicated by the signal of the $v1$ symmetric C–H stretching vibration at around 2920 cm^{-1}; the C_2H_6 is indicated by the $v1$ symmetric CH_3 stretching vibration at around 2958 cm^{-1} and a complex Fermi resonance in the C–H stretching at 2902 cm^{-1}; the C_3H_8 is indicated by the peak at 2888 cm^{-1}, 2932 cm^{-1} and 2975 cm^{-1}; the nC_4H_{10} indicated by the peak at 2889 cm^{-1} and 2948 cm^{-1}, the iC_4H_{10} is indicated by the –CH_3 torsional vibration at 2878 cm^{-1}; the C_2H_4 is indicated by the signal of C–H and C–C symmetric stretching vibration at 3025 cm^{-1}. The Raman signals of CO_2 at the lower band of 1284 cm^{-1} and the upper band of 1387 cm^{-1} were not obtained in any of the anhydrous FSCCs.

ated after 10-d heating, particularly in the systems with clay minerals (Fig. 2e–f), and the relative intensity of the Raman signals suggests a relatively higher ratio of C_1/C_2 and C_1/C_{3+4}. In the $nC_{16}H_{34}$-quartz experiments (I-b), similar to the I-a system without minerals, clear signals of C_1-nC_4 alkanes and ethene were detected only after 10-d heating (Fig. 2b).

In the $nC_{16}H_{34}$-D water systems, various hydrocarbon gases were generated and Raman signals of the C_1-nC_4 alkanes in the II-a FSCC (Supplementary data, Fig. S2a1) were much stronger than in the I-a FCSS (Fig. 2a2) after 6–10 d heating, consistent with the yields' relation in the gold capsules (Fig. 1a, b). The presence of quartz in the FSCC (II-b) resulted in slightly weaker Raman signals of the gaseous alkanes (Supplementary data, Fig. S2a2) than in the II-a FSCC without minerals, particularly the signals of methane and ethane. In contrast, the presence of other minerals (II-c/d/e/f/g), particularly the calcite and clay minerals in the FSCCs resulted in stronger Raman signals of the gaseous alkanes, which could be detected clearly after only 3-d heating (Supplementary data, Fig. S2a3–a7). The signals became more stronger in the 6–10 d heating experiments. Consistent with the gold capsules, comparisons of the intensity of Raman peaks between the hydrous systems with D water (Supplementary data, Fig. S2a1–a7) and the anhydrous systems (Fig. 2a2–g2) also suggest higher ratios of C_1/C_2 and C_1/C_3 in the hydrous system.

Consistent with the gold capsules, comparison of the intensive of Raman signals in the III-a, I-a and II-a FSCCs suggest that the $nC_{16}H_{34}$-$CaCl_2$ water system (III-a) generate lower amounts of gaseous hydrocarbons (Supplementary Fig. S2b1) than the II-a FSCC with D-water (Supplementary data, Fig. S2a1), but the Raman signals of the gaseous alkanes were stronger than in the I-a anhydrous FSCC after 10-d heating (Fig. 2a2). Similar to the system with D water, the presence of quartz in the FSCC (III-b) resulted in weaker Raman signals of the gaseous alkanes (Supplementary data, Fig. S2b2) than in the III-a FSCC without minerals (Supplementary data, Fig. S2b1). The presence of calcite (III-d) and clay minerals (III-e/f/g) resulted in stronger Raman signals of the gaseous alkanes (Supplementary data, Fig. S2b4-b7) that could be detected clearly after 6-d heating, but still much weaker than that in the systems with D water (Supplementary data, Fig. S2a4-a7). Similar to the gold capsule, the presence of feldspar in the hydrous FSCC with $CaCl_2$ water also had little impact on gas generation (Supplementary data, Fig. S2b3). Similar to the hydrous system with D water, higher ratios of C_1/C_2 and C_1/C_3 existed in the hydrous systems with $CaCl_2$ water (Supplementary data, Fig. S2b1-b7) than the anhydrous systems (Fig. 2a2–g2), as suggested by the intensity of the Raman signals.

Besides the differences between the different systems, the Raman spectra patterns and relative intensity of different Raman peaks of the same system also varied gradually as the heating time lasted from 3 d to 10 d. And comparisons suggest that the Raman peak intensity of C_1 and C_2 increased faster than that of C_3 and C_4 in the present experiments (Fig. 2; Supplementary data, Fig. S2).

3.1.3. Raman spectra of CO_2 and H_2 in the FSCCs

For non-hydrocarbon gases, CO_2 was not detected in any of the anhydrous FSCCs (Fig. 2a1–g1), consistent with the gold capsules (Fig. 1a; Supplementary data, Table S4). In contrast to the anhydrous systems, the laser Raman peaks of CO_2 were identified by the Fermi diad at 1284 cm^{-1} and 1387 cm^{-1} (Chou et al., 2008) in most hydrous FSCC systems in the present study and two hot band signals appeared in some Raman spectra (Supplementary Fig. S3). In the $nC_{16}H_{34}$-D water system (II-a) and the $nC_{16}H_{34}$-$CaCl_2$ water system (III-a), the CO_2 did not increase noticeably as the heating lasted from 3 d to 10 d, but a small bulge was identified near 1387 cm^{-1} (Supplementary Fig. S3a1, b1). With the addition of feldspar (II-c), calcite (II-d), and clays (II-e-g), the concentration of CO_2 increased noticeably in the FSCCs from 3 d to 10 d, and two peaks at 1284 cm^{-1} and 1387 cm^{-1} were identified clearly after heating of 6–10 d (Supplementary data, Fig. S3a3-a7). In contrast, the Raman signal of CO_2 was not detected obviously in the systems with quartz (II-b, III-b), even after 10-d heating (Supplementary data, Fig. S3a2, b2). A comparison of the results showed that the FSCCs with calcite had the strongest CO_2 signal, followed by the FSCCs with clays, and the FSCC with feldspar. Different from the results in gold capsules, the Raman signal of H_2 was not identified in any of the present FSCC experiments, which was probably due to the highly permeable of the silica tube to H_2 (Chou et al., 2008; Shang et al., 2009).

3.2. Liquid hydrocarbons and pyrobitumen

3.2.1. Gas chromatograms of liquid hydrocarbons in the gold capsules

After the 10-d heating, the GC analysis of the liquid hydrocarbons in the different gold capsules showed that the pure $nC_{16}H_{34}$ evolved to form both LMW organics (nC_6-nC_{15} and mono-bicyclic aromatic hydrocarbons (M-BAHs)) and high-molecular-weight (HMW) organics (nC_{17}-nC_{30} and polycyclic aromatic hydrocarbons (PAHs) ($\geq$3 rings)), and the products varied significantly in different systems (Fig. 3).

In the I'-a anhydrous system, newly generated liquid hydrocarbons included primarily nC_6-$nC_{15,}$ nC_{17}-$nC_{30,}$ and some HMW PAHs (Fig. 3a1). Comparisons showed that the addition of quartz, feldspar, and calcite into the anhydrous system led to generation of more HMW organics (Fig. 3a2-a4) than in the system without minerals (Fig. 3a1), and the quartz, feldspar and calcite had slight impact on the generation of nC_6-nC_{15}. In contrast, the anhydrous systems with addition of clay minerals (particularly kaolinite and smectite) generated much less HMW organics but much more nC_6-nC_{15} and M-BAHs than the anhydrous system without mineral (Fig. 3a5–a7).

Comparison of the gas chromatograms show that much less HMW organics were produced in the hydrous systems with D-water (II'-a) (Fig. 3b1) than in the anhydrous system (Fig. 3a1). What's more, the presence of quartz, feldspar, calcite, kaolinite, and smectite in the FSCCs generated more nC_6-nC_{15} and less HMW organics (Fig. 3b2–b6) than in the $nC_{16}H_{34}$-D water system (Fig. 3b1). In the $nC_{16}H_{34}$-D water-illite system, slightly more C_{19}-C_{26} organics (Fig. 3b7) were generated than in the $nC_{16}H_{34}$-D water system (Fig. 3b1), but the amount was still much less than in the I'-g anhydrous system without water (Fig. 3a7).

Similar to the hydrous systems with D water, less HMW organics were produced in the $nC_{16}H_{34}$-$CaCl_2$ water system (Fig. 3c1) than in the anhydrous system (Fig. 3a1). The presence of minerals including feldspar, calcite and clays also resulted in much more generation of LMW alkanes (nC_6-nC_{13}) (Fig. 3c3–c7) than the system without minerals (III'-a) (Fig. 3c1). Regarding HMW organics, however, the presence of minerals tended to generate more HMW organics (Fig. 3c3–c7) than the system without mineral, but the ratios of HMW organics/LMW organics were still lower than the system without minerals (Fig. 3c1).

3.2.2. Fluorescence colors and spectra of liquid hydrocarbons in the FSCCs

The pure colorless $nC_{16}H_{34}$ and the transparent FSCCs prior to the experiments showed no fluorescence color under UV light. After 3–10 d heating, however, different fluorescence colors were identified in the different systems and in the same system at different times (Figs. 4-5; Supplementary Figs. S4-S5) due to differences of the liquid hydrocarbon compositions (Fig. 3) (Bourdet et al., 2012, 2014; Liu et al., 2014; Cheng et al., 2019).

In the anhydrous I-a $nC_{16}H_{34}$ system without minerals, the fluorescence colors of liquid hydrocarbons in the 3-d, 6-d, and 10-d

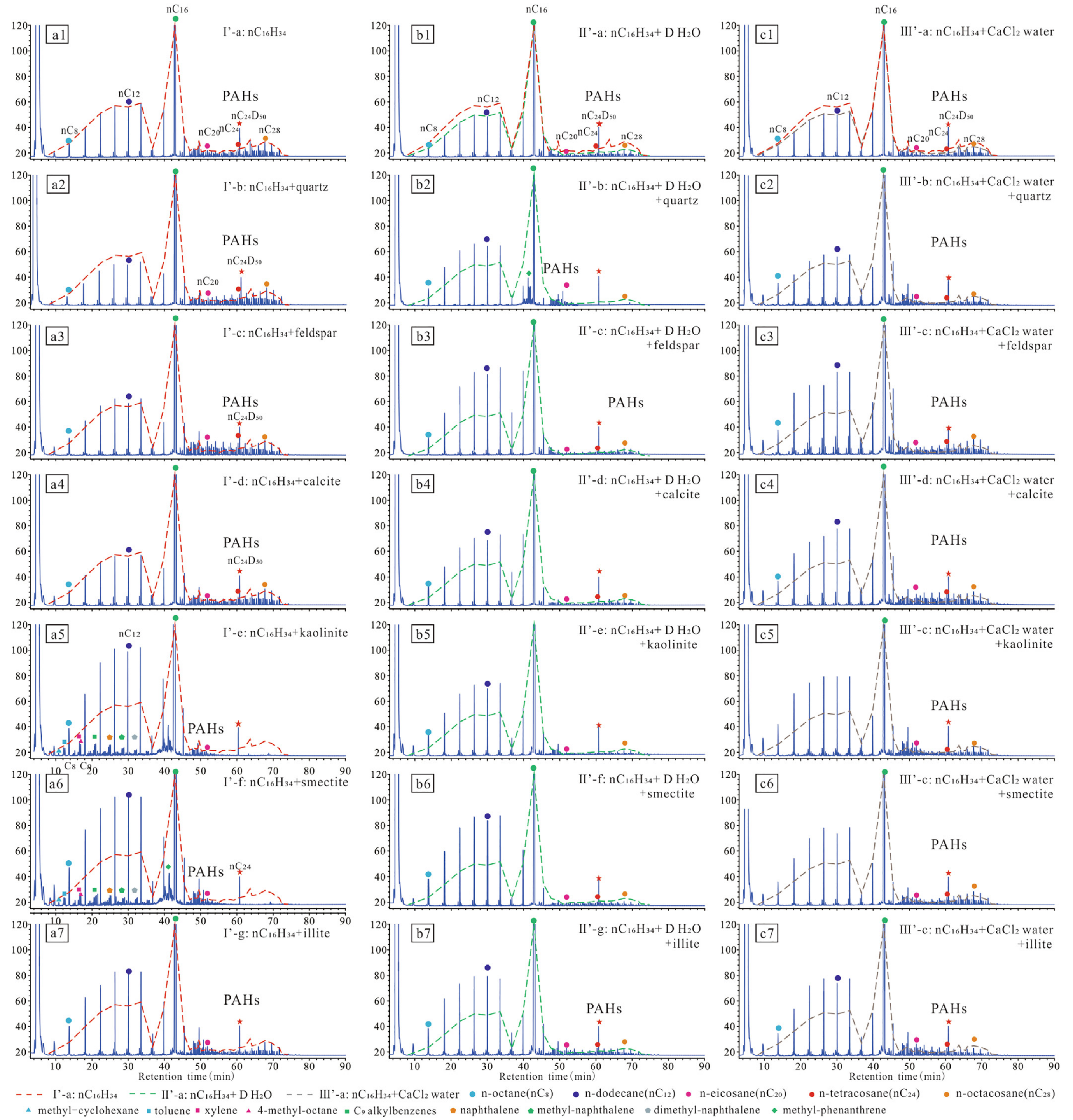

Fig. 3. Gas chromatograms of the liquid hydrocarbons in the anhydrous $nC_{16}H_{34}$ systems (a1–a7), hydrous systems with D water (b1–b7) and hydrous systems with $CaCl_2$ water (c1–c7) after 10-d heating. The red, green and orange dashed curves represent the patterns of the main compositions of the liquid hydrocarbons in the I'-a, II'-a and III'-a systems after the experiments, respectively. Besides obvious signals of *n*-alkanes, peaks representing M-BAHs (toluene, xylene, C_9 alkylbenzenes, naphthalene, methyl-naphthalene, dimethyl-naphthalene) (after Pan et al., 2009; Yuan et al., 2019b) and PAHs (methyl-phenanthrene, and others with more carbons) can also be identified clearly in the gas chromatograms.

FSCCs became stronger gradually, and the colors changed from weak dark blue to blue and strong yellow-white (Fig. 4a1–a3). The λ_{max} (520.38 → 515.53 → 518.67), $Q_{650/500}$ (0.31 → 0.19 → 0.20) and QF_{535} (0.96 → 0.72 → 0.83) values of the fluorescence spectra decreased from 3-d to 6-d and then increased in the 10-d FSCC (Fig. 5a1–a3; Supplementary data, Table S5). The peak near 433 nm in the 10-d experiment was much lower than that in the 3-d and 6-d experiments (Fig. 5a1–a3), indicating the generation of more HMW organics (Fig. 3a1). In the FSCCs with the presence of quartz (I-b), feldspar (I-c), and calcite (I-d), the fluorescence colors changed from 3-d blue to 6-d white-blue and yellow, and 10-d strong white-yellow to yellow–brown (Fig. 4b1–d3). Particularly, the liquid hydrocarbons in the 10-d FSCCS exhibited yellow to brown colors under transmitted light. The values of λ_{max}, $Q_{650/500}$ and QF_{535}

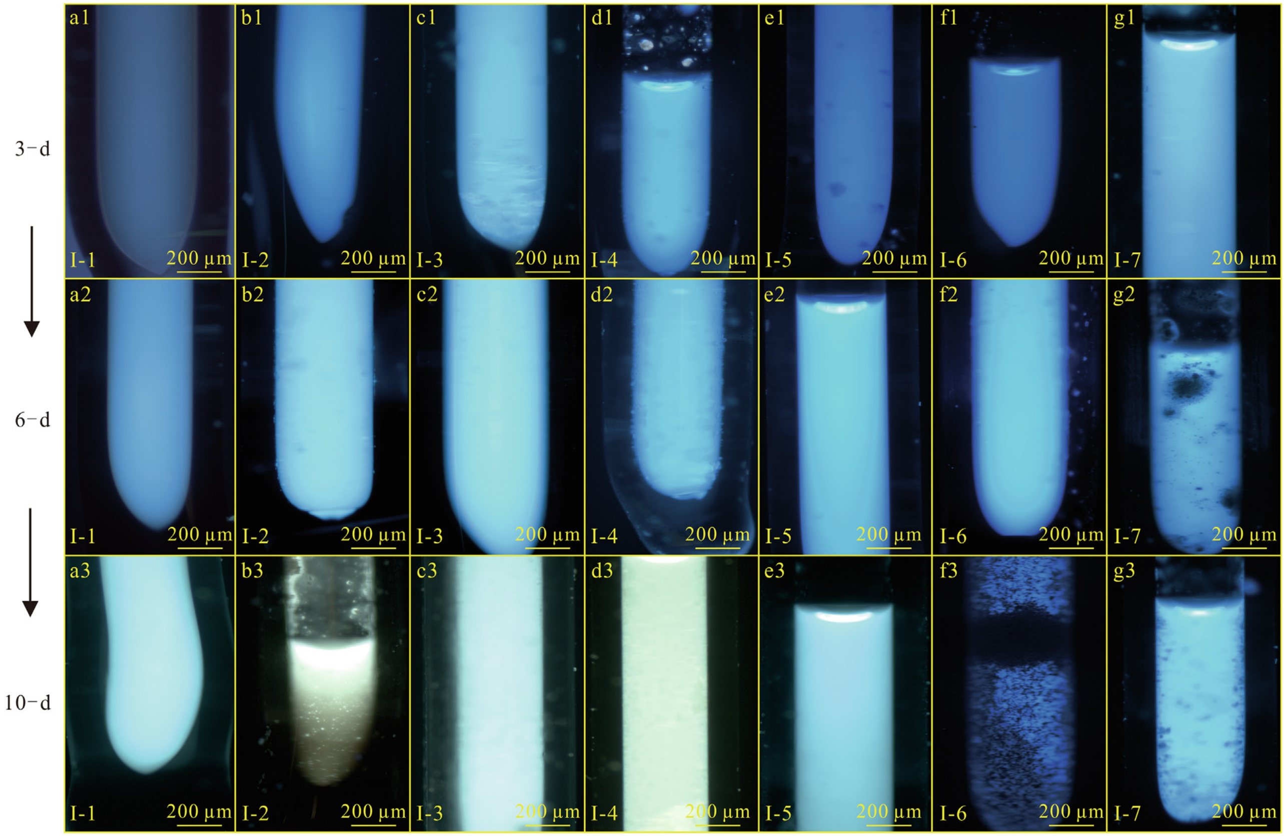

Fig. 4. Photomicrographs showing fluorescence colors of the liquid hydrocarbons in the Series-I anhydrous FSCCs (I-1: a1-a3, I-2: b1-b3, I-3: c1-c3, I-4: c1-c3, I-5: e1-e3, I-6: f1-f3, I-7: g1–g3). Photomicrographs (a1–g1) from the 3-d experiments, (a2–g2) from the 6-d experiments, and (a3–g3) from the 10-d experiments.

of the fluorescence spectra in the I-b/c/d systems increased as the experiments continued, particularly for the 10-d experiments (Supplementary Table S5). The continuous red-shift of the fluorescence spectra (Fig. 5a1–a3) indicated an increase in concentrations of HMW organics, consistent with the gas chromatograms (Fig. 3a2–a4) (Bourdet et al., 2012, 2014; Liu et al., 2014; Cheng

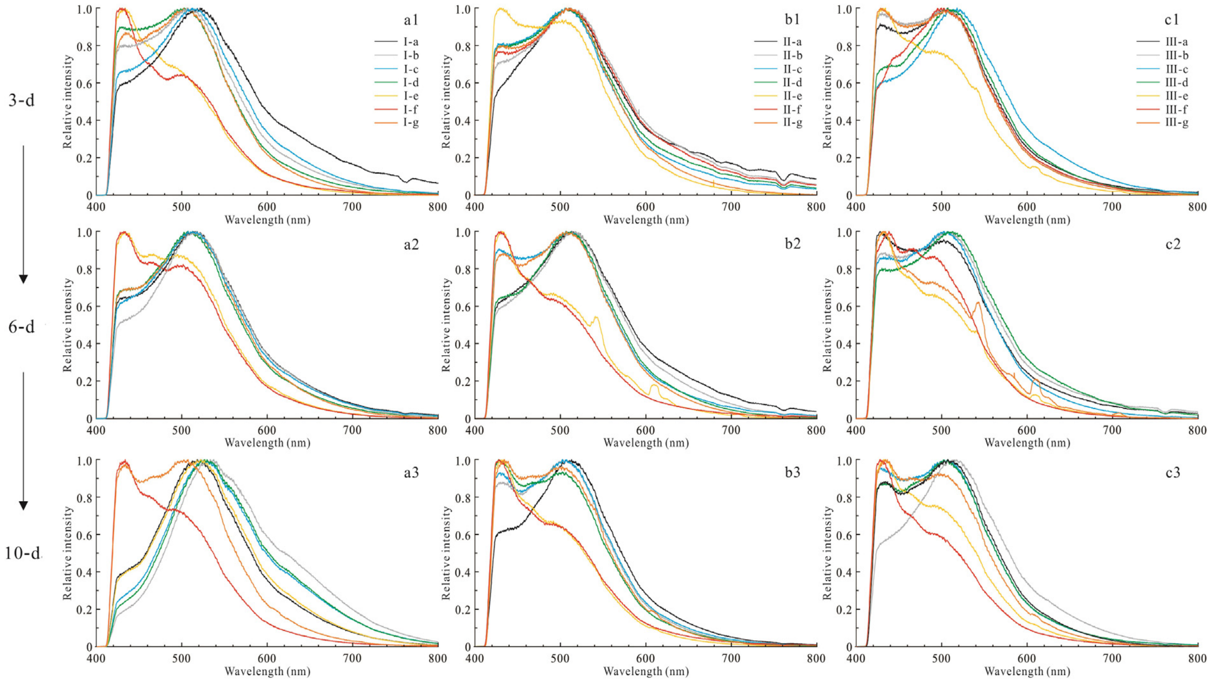

Fig. 5. Fluorescence spectra of liquid hydrocarbons in all the FSCCs after 3-d, 6-d and 10-d heating. (a1–a3) $nC_{16}H_{34}$-mineral systems; (b1–b3) $nC_{16}H_{34}$-D water–mineral systems; (c1–c3) $nC_{16}H_{34}$-$CaCl_2$ water–mineral systems. (a1–c1) 3-d experiments; (a2–c2) 6-d experiments; (a3–c3) 10-d experiments.

et al., 2019). In contrast, the presence of clays resulted in the formation of blue, blue-white, and white blue fluorescence colors of the liquid hydrocarbons, and the fluorescence colors became stronger as the experiments continued (Fig. 4e3–g3). The values of λ_{max}, $Q_{650/500}$, and QF_{535} of the fluorescence spectra remained almost stable as the experiments continued from 3 d to 10 d, and these values were much lower than the I-a system (Supplementary data, Table S5), suggesting strong blue-shift of the fluorescence spectra compared to the I-a system, particularly in the system with smectite. In addition, the peak near 433 nm was higher than the peak near 520 nm in the FSCCs with smectite and kaolinite (Fig. 5a1–a3). The blue-shift of the fluorescence spectra indicated an increase in concentrations of LMW organics, consistent with the gas chromatograms (Fig. 3a5–a7) (Bourdet et al., 2012, 2014; Liu et al., 2014; Cheng et al., 2019).

In the hydrous systems with D water (Series-II) and $CaCl_2$ water (Series-III), the fluorescence colors of the generated liquid hydrocarbons differ significantly from that of the anhydrous Series-I systems (Fig. 4), and no yellow-white, yellow and yellow–brown fluorescence colors were identified in relevant FSCCs (Supplementary data, Figs. S4 andS5). In the $nC_{16}H_{34}$-D water systems (II-a), the fluorescence colors changed from an extremely weak fluorescence color in the 3-d experiment to weak-blue and blue in the 6-d and 10-d experiments (Supplementary data, Fig. S4a1–a3). The fluorescence spectra of the liquid hydrocarbons exhibited similar λ_{max} values (511–513 nm) and the $Q_{650/500}$ and QF_{535} values decreased gradually as the heating lasted from 3 d to 10 d (Fig. 5b1–b3; Supplementary data, Table S5). These values were lower than that in the anhydrous system (I-a), and no sharp intensity decrease was identified around the 433 nm peak (Fig. 5b3) after 10-d heating, suggesting blue-shift of the fluorescence spectra when compared to that in the anhydrous systems (Fig. 5a3, b3). With the addition of different minerals, the fluorescence colors became stronger than in the hydrous system without minerals after heating for the same time, and the colors were blue and white-blue after 6–10 d heating (Supplementary data, Fig. S4b1-g3). With the addition of different minerals to the series-II systems, the intensity of the peak at 433 nm increased significantly, and the values of λ_{max}, $Q_{650/500}$, and QF_{535} declined a lot compared to the systems without minerals (Fig. 5b1–b3; Supplementary data, Table S5). The fluorescence spectra of the liquid hydrocarbons in the FSCCs with minerals (II-b/c/d/e/f/g) demonstrated a strong blue-shift when compared to the II-a system without minerals (Fig. 5b1–b3; Supplementary Table S5); the blue shift became stronger as the experiments continued (Supplementary data, Table S5), indicating generation of more LMW organics (Fig. 3b2–b7) (Bourdet et al., 2012, 2014; Liu et al., 2014; Cheng et al., 2019). In addition, comparisons among the systems with different minerals after heating for the same time showed that the most extensive blue-shift of the fluorescence spectra occurred in the presence of smectite and kaolinite, followed by illite, feldspar, and calcite (Fig. 5b1–Bb3; Supplementary data, Table S5). The weakest blue-shift occurred in the system with quartz.

In the $nC_{16}H_{34}$-$CaCl_2$ water system (III-a), the fluorescence colors changed from weak blue fluorescence to blue in the 6–10 d experiments (Supplementary data, Fig. S5a1–a3). The fluorescence spectra of the liquid hydrocarbons were different from those of the anhydrous I-a system and the hydrous II-a system with D water (Fig. 5; Supplementary data, Table S5). Two peaks near 420 nm and 507 nm were present in the spectra (Fig. 5c1–c3). The λ_{max}, $Q_{650/500}$, and QF_{535} values were lower than in the I-a systems, and the fluorescence spectra exhibited a blue-shift when compared to the I-a systems (Fig. 5; Supplementary data, Table S5), indicating the generation of more LMW liquid hydrocarbons in the presence of $CaCl_2$ water than in the anhydrous systems.

With the addition of quartz (III-b), feldspar (III-c), and calcite (III-d), the λ_{max} remained high after heating for 10 d, and the $Q_{650/500}$ and QF_{535} values were higher than in the III-a system (Supplementary data, Table S5), the fluorescence spectra of the liquid hydrocarbons exhibited slightly red-shift (Fig. 5c1–c3) when compared to the III-a system, indicating the generation of more HMW liquid organics (Fig. 3c2–c4). In contrast, in the experiment with kaolinite (III-e), smectite (III-f), and illite (III-g), the fluorescence spectra of the liquid hydrocarbons exhibited a strong blue-shift compared to the III-a system (Fig. 5c1–c3), and the values of λ_{max}, $Q_{650/500}$ and QF_{535} were lower than in the III-a system (Supplementary data, Table S5).

3.2.3. Heavy oil and pyrobitumen produced in the FSCCs

The presence of heavy oil and pyrobitumen on the surfaces of different minerals and the FSCCs was identified using a microscope with UV light (Fig. 6). The photomicrographs show that heavy oil was attached to the tube wall in the anhydrous $nC_{16}H_{34}$ experiment (Fig. 6a1-a2), and pyrobitumen was identified on some surfaces of the smectite (Supplementary data, Fig. S5b1-b2), illite (Fig. 6c1-c2), kaolinite (Fig. 6d1-d2) and feldspar (Fig. 6e1-e2) in the anhydrous alkane-mineral systems after 10-d heating; this was particularly noticeable in the anhydrous I-f system with smectite and the anhydrous I-g system with illite (Fig. 6b1-c2). Different from the anhydrous systems, in the hydrous systems with D water or $CaCl_2$ water, heavy oil or pyrobitumen were rarely observed on the mineral surfaces or the tube wall, even in the FSCCs after 10-d heating (Supplementary data, Fig. S4-S5).

3.3. Organics detected in the water in the FSCCs

The Raman spectra of the water solutions in the two series of hydrous systems with D water (series-II) and $CaCl_2$ water (series-III) after 3–10 d heating are presented in Fig. 7. Comparisons of the Raman spectra of the water solutions after heating (Fig. 7a1-a7, b1-b7) to those of the initial D water (Fig. 7a0) and $CaCl_2$ water (Fig. 7b0) show that oxygen-containing organics (2800–3000 cm^{-1}) were present in the water solutions after heating for 6–10 d. Methanol (2885 cm^{-1} and 2956 cm^{-1}), ethanol (2936 cm^{-1} and 2847 cm^{-1}) (Chou et al., 2008; Xu abd Chou, 2017; Wang et al., 2018), and acetic acid (2944 cm^{-1}) (Zou et al., 2007; Chou et al., 2008) were identified, particularly the ethanol and acetic acid (Fig. 7). The intensity of the Raman signal peaks became stronger as the heating lasted from 3 d to 10 d, indicating more generation of the oxygen-containing organics in the FSCCs.

In the presence of feldspar (Fig. 7a3, b3), calcite (Fig. 7a4, b4), kaolinite (Fig. 7a5, b5), and illite (Fig. 7a7, b7), the intensity of the Raman signals of the oxygen-containing organics in the water solutions in the series-II and series-III systems showed slightly difference with those of the systems without minerals (Fig. 7a1, b1). When quartz (Fig. 7a1, b1) and smectite (Fig. 7a6, b6) were added to the hydrous systems with D-water and $CaCl_2$ water, however, the intensity of the Raman signals of the oxygen-containing organics became slightly weaker.

3.4. Mineral alteration in various systems

After experiments, various mineral alterations were identified in the different anhydrous and hydrous systems with different minerals, and the different mineral textures were presented in Fig. 8 and Supplementary data, Fig. S6-S7.

3.4.1. In anhydrous systems

The SEM images show that for the quartz (Supplementary data, Fig. S6a, a1), feldspar (Supplementary data, Fig. S6b, b1) and calcite (Supplementary data, Fig. S6c, c1) minerals without structure or

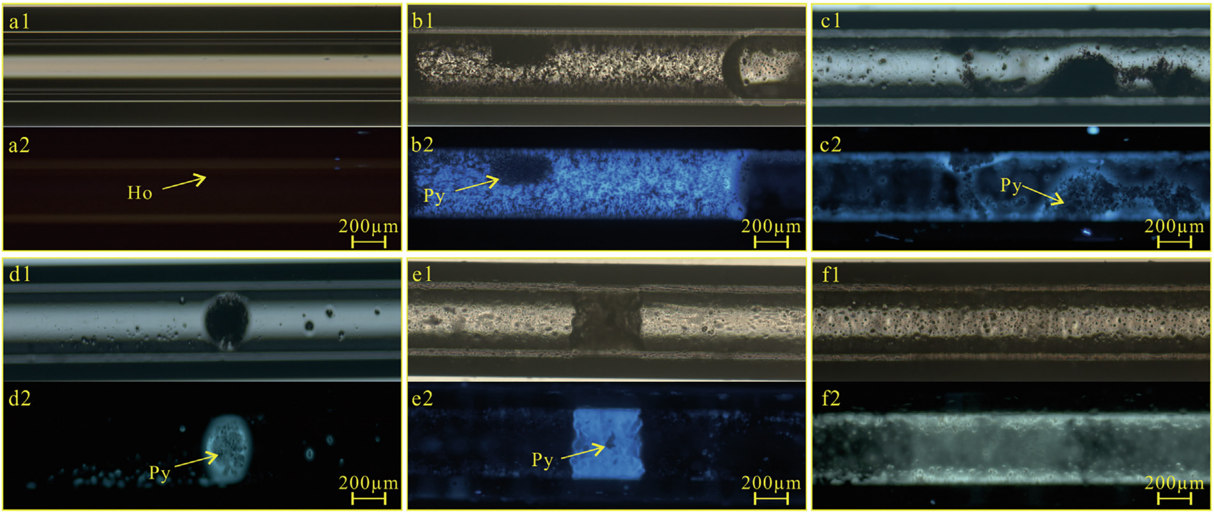

Fig. 6. Photomicrographs of pyrobitumen and heavy oil in different FSCCs. (a1, a2) Heavy oil attached to the tube wall after 10-d heating in the anhydrous alkane systems (I-a). (b1, b2) Pyrobitumen attached to the smectite surface in the I-f system after 10-d heating. (c1, c2) Pyrobitumen attached to the illite surface in the I-g system after 10-d heating. (d1, d2) Heavy oil and pyrobitumen attached to the kaolinite surface in the I-e system after 10-d heating. (e1, e2) Pyrobitumen attached to the feldspar surface in the I-c system after 10-d heating. (f1, f2) No pyrobitumen was identified on the silica surface after 10-d heating. Ho: heavy oil; Py: pyrobitumen. (a1–f1) Acquired under transmitted light, (a2–f2) acquired under UV light.

interlayer waters (Supplementarydata, Fig. S8a-c), the mineral morphology showed no difference before and after the heating experiments in the anhydrous systems. The grain surfaces of these three minerals prior to and after the experiments were relatively flat, and no leaching pits or pores were identified in these minerals in the 3–10 d experiments; no secondary minerals were generated (Supplementary data, Fig. S6a-c). Similarly, the kaolinite (Supplementary data, Fig. S6d, d1) and illite (Supplementary data, Fig. S6f, f1) with structured water (Supplementary data, Fig. S8d, f) also exhibited no apparent alteration after the heating, and no secondary minerals were identified, even after the 6–10 d heating. Unlike the other minerals, the smectite with interlayer water (Supplementary data, Fig. S8e) exhibited apparent differences after the reactions (Supplementary data, Fig. S6e, e1); more pits were identified in the smectite after the reactions although typical euhedral secondary minerals were not identified after heating.

3.4.2. In hydrous systems

In contrast to the anhydrous system, the SEM images showed various mineral alterations after heating for 3–10 days in the hydrous systems (Fig. 8; Supplementary data, Fig. S7). Overall, the calcite and feldspar experienced the most extensive alterations, followed by smectite, kaolinite, quartz, and illite.

In the hydrous systems with quartz, a large number of small leaching pits were identified on the quartz surfaces in both the systems with D water and $CaCl_2$ water (Fig. 8a, b). In addition, some anhedral calcite grains (Fig. 8c) were precipitated in the systems with $CaCl_2$ water after heating for 6–10 d. In both the hydrous systems with D water and $CaCl_2$ water, extensive mineral alteration of feldspar was identified. In the first three days, feldspar dissolution (Fig. 8d, g) was the most important reaction; after heating for 6–10 d, secondary illite (Fig. 8e, f, h) was identified in both systems, with additional development of anorthite (Fig. 8i) in the systems with $CaCl_2$ water. Calcite was dissolved extensively in the hydrous systems after three days (Fig. 8j). In the 3-d experiments, reprecipitation of calcite was weak in the system with D water (Fig. 8j), but extensive in the system with $CaCl_2$ water (Fig. 8k); in the 6–10 d experiments, calcite dissolution and reprecipitation were extensive in both the systems with D water and $CaCl_2$ water (Fig. 8l).

In the kaolinite, leaching pits and gulfs were identified on the mineral surfaces in the hydrous systems (Supplementary data, Fig. S7a, b), particularly in the system with $CaCl_2$ water (Supplementary data, Fig. S7c). No typical secondary minerals were identified in the D water system, even after 6–10 d heating; however, scaly secondary minerals without euhedral crystals were formed in the systems with $CaCl_2$ water (Supplementary data, Fig. S7c). In the smectite, leaching pits were identified in the hydrous systems with both D water and $CaCl_2$ water (Supplementary data, Fig. S7d, g). After reacting for 6–10 d, illitization of smectite was clearly identified, and fibrous illite adhered to the remnant smectite (Supplementary data, Fig. S7e, f, h). In addition, some anhedral calcite was identified after 6–10 d reaction in the systems with $CaCl_2$ water (Supplementary Fig. S7i). Although some pits were identified on the surfaces of the illite mineral, no typical secondary minerals were identified, even after 6–10 d heating (Supplementary data, Fig. S7j-l). Recrystallization may have occurred; however, it was difficult to determine this alteration in the SEM images.

4. Discussion

Results of the present experiments indicate that various organic–inorganic interactions occurred in the different hot systems with different $nC_{16}H_{34}$-water–mineral assemblages. On the whole, the reaction pathways relevant to organics include free-radical thermal-cracking and free-radical cross-linking in all the systems, step oxidation of hydrocarbons and decarboxylation of organic acids in the hydrous systems (Lewan, 1997; Seewald, 2001, 2003; Wang et al., 2016; Yuan et al., 2019b), and an obvious carbonium-ion pathway in the systems with the presence of clays. Inorganic reactions include mainly the dissolution and precipitation of different minerals in the different hydrous systems (van Berk et al., 2015; Yuan et al., 2019b). The presence of different water and minerals affect the $nC_{16}H_{34}$ degradation processes, which in turn affect the mineral alteration reactions. Besides, the water type also affected the impact of the different minerals on $nC_{16}H_{34}$ degradation, via its impact on mineral alteration processes. Coupled together, different organic–inorganic reactions evolved following different reaction pathways and resulted in generation of the different products (Figs. 9, 10).

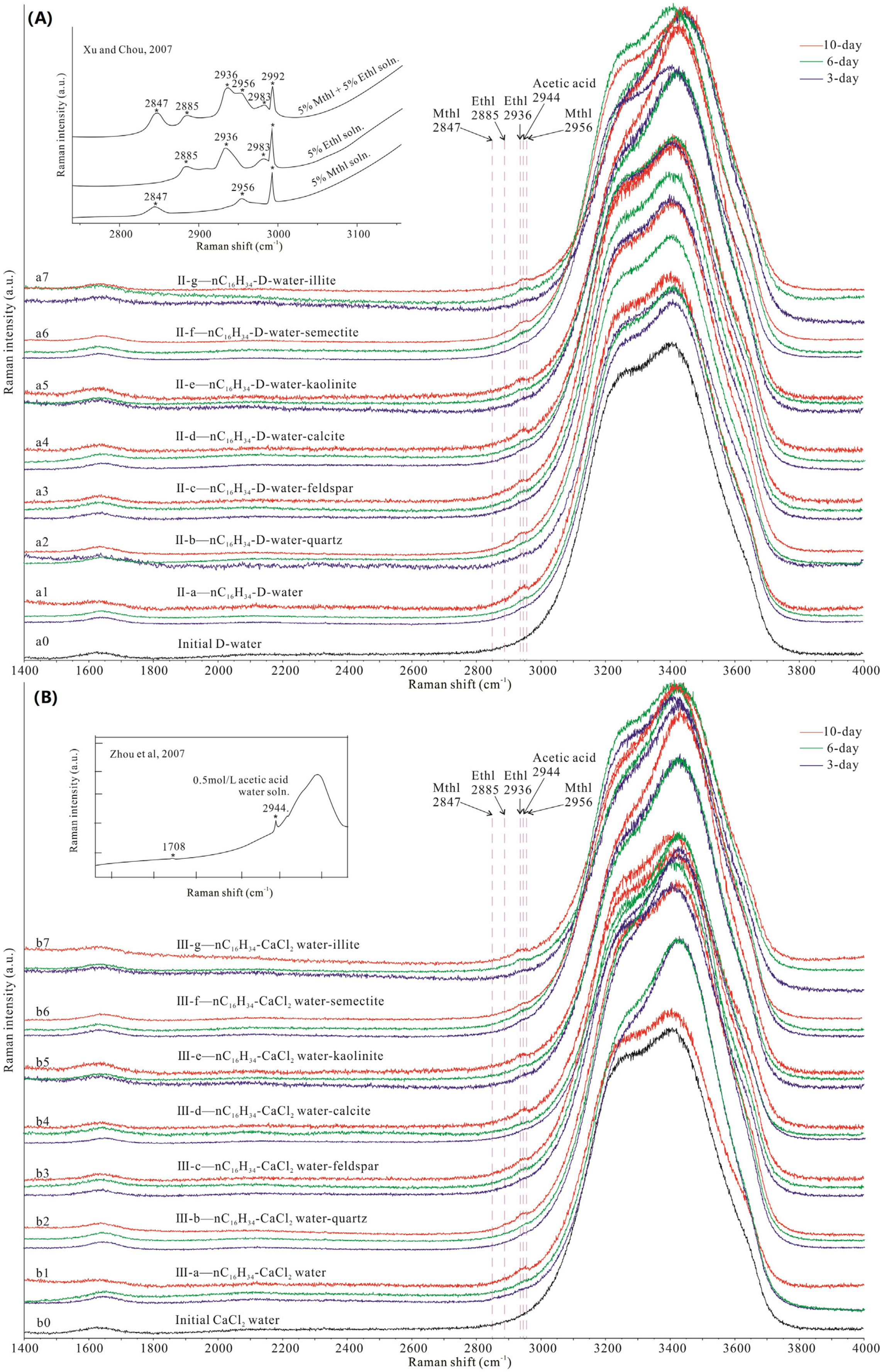
(A)
Xu and Chou, 2007
Raman intensity (a.u.)
2847
2885
2936
2956
2983
2992
5% Mthl + 5% Ethl soln.
5% Ethl soln.
5% Mthl soln.
2800
2900
3000
3100
Raman shift (cm^{-1})
10-day
6-day
3-day
Mthl 2847
Ethl 2885
Ethl 2936
Acetic acid 2944
Mthl 2956
Raman intensity (a.u.)
a7 II-g—nC$_{16}$H$_{34}$-D-water-illite
a6 II-f—nC$_{16}$H$_{34}$-D-water-semectite
a5 II-e—nC$_{16}$H$_{34}$-D-water-kaolinite
a4 II-d—nC$_{16}$H$_{34}$-D-water-calcite
a3 II-c—nC$_{16}$H$_{34}$-D-water-feldspar
a2 II-b—nC$_{16}$H$_{34}$-D-water-quartz
a1 II-a—nC$_{16}$H$_{34}$-D-water
a0 Initial D-water
1400
1600
1800
2000
2200
2400
2600
2800
3000
3200
3400
3600
3800
4000
Raman shift (cm^{-1})
(B)
Zhou et al, 2007
Raman intensity (a.u.)
0.5mol/L acetic acid water soln.
2944
1708
Raman shift (cm^{-1})
10-day
6-day
3-day
Mthl 2847
Ethl 2885
Ethl 2936
Acetic acid 2944
Mthl 2956
Raman intensity (a.u.)
b7 III-g—nC$_{16}$H$_{34}$-CaCl$_2$ water-illite
b6 III-f—nC$_{16}$H$_{34}$-CaCl$_2$ water-semectite
b5 III-e—nC$_{16}$H$_{34}$-CaCl$_2$ water-kaolinite
b4 III-d—nC$_{16}$H$_{34}$-CaCl$_2$ water-calcite
b3 III-c—nC$_{16}$H$_{34}$-CaCl$_2$ water-feldspar
b2 III-b—nC$_{16}$H$_{34}$-CaCl$_2$ water-quartz
b1 III-a—nC$_{16}$H$_{34}$-CaCl$_2$ water
b0 Initial CaCl$_2$ water
1400
1600
1800
2000
2200
2400
2600
2800
3000
3200
3400
3600
3800
4000
Raman shift (cm^{-1})

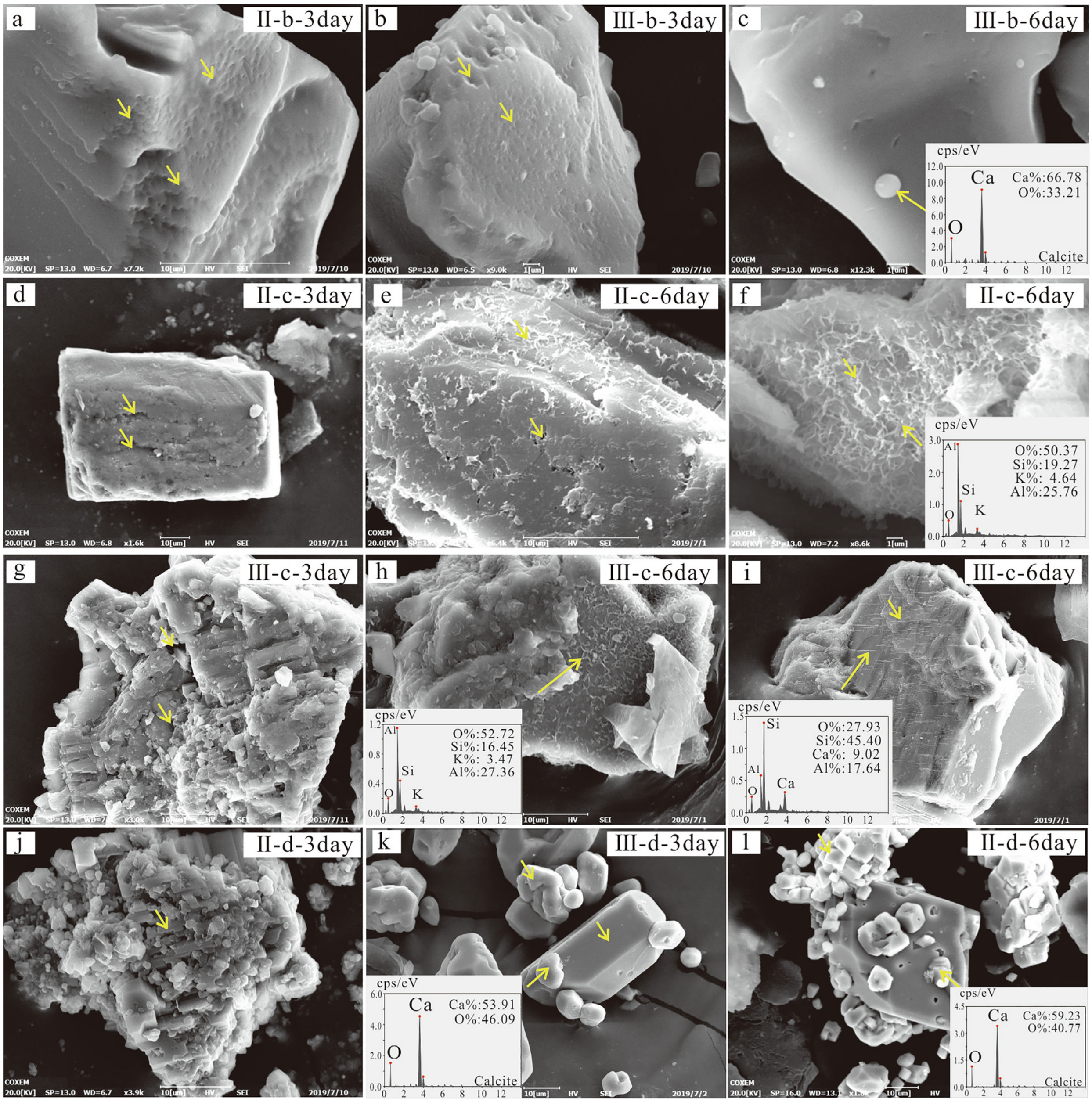

Fig. 8. Microphotos of leached minerals and authigenic minerals in the hydrous FSCCs with quartz, feldspar and calcite. (a, b) Leaching pits on the quartz surfaces; (c) anhedral calcite precipitated on the quartz surfaces; (d) leached feldspar grain; (e, f) leached feldspar grain and fibrous illite precipitated on the feldspar surfaces; (g) leached feldspar grain; (h) leached feldspar and fibrous illite precipitated on the feldspar surface; (i) anorthite formed by replacement of K-feldspar; (j) extensively leached calcite; (k, l) leached calcite and reprecipitated calcite on the calcite grain surfaces.

4.1. Reaction pathways of organic–inorganic interactions in anhydrous systems

4.1.1. Anhydrous $nC_{16}H_{34}$ system without minerals

Many studies have verified that hydrocarbon degradation in anhydrous systems proceeds through the free radical mechanism (Lewan, 1997; Hill et al., 2003; Tian et al., 2006; Yuan et al., 2019b). In this study, the extremely low amounts of iC_4 and iC_5 (Supplementary data, Table S4; Fig. 1a), the wide distribution of the LMW *n*-alkanes (C_1-C_{15}) (Fig. 3a1), and the enrichment of lower-molecular-weight alkane gases in the anhydrous system (Fig. 2a2) with on-going heating support extensive occurrence of the free-radical thermal-cracking reaction (Fig. 9a). The presence of the HMW alkanes (C_{17}-C_{30}), PAHs, and H_2 in the I'-a gold capsule

Fig. 7. Raman spectra of the aqueous phases of the hydrous systems with D-water (A) and $CaCl_2$ water (B) after 3-d. 6-d and 10-d heating. The Raman peaks of methanol are near 2847 cm^{-1} and 2956 cm^{-1}, the Raman peaks of ethanol are near 2885 cm^{-1} and 2936 cm^{-1}, and the Raman peak of acetic acid is near 2944 cm^{-1} (after Zou et al., 2007; Chou et al., 2008; Wang et al., 2016; Xu and Chou, 2017). For comparison, the Raman spectra of the initial D water and $CaCl_2$ water are presented.

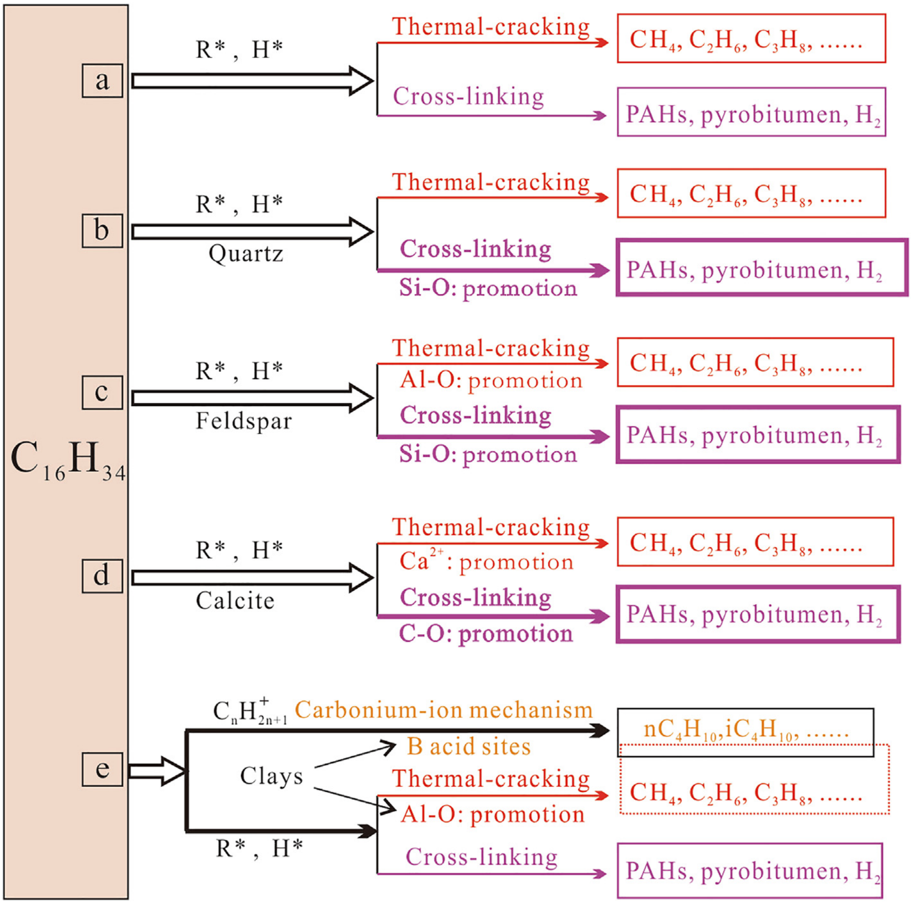

Fig. 9. Possible reaction pathways of organic–inorganic interactions and products in different $nC_{16}H_{34}$-mineral systems.

(Fig. 1a and 3a1), and M-BAHs with weak blue fluorescence colors and PAHs with yellow-white fluorescence colors in the I-a FSCCs from 3 to 10 d heating (Fig. 3a1; Fig. 4a1–a3) demonstrated the occurrence of free-radical cross-linking reaction during the $nC_{16}H_{34}$ degradation processes (Lewan, 1997; Yuan et al., 2019b). Step oxidation and decarboxylation reactions (Seewald, 2003) was ruled out by the absence of CO_2 in the generated gases (Fig. 1a and 2a1). Thus, the free-radical thermal-cracking reaction and free-radical cross-linking reaction dominate the present anhydrous $nC_{16}H_{34}$ degradation. As evidenced by the gradual enrichment of LMW gases and HMW PAHs in the FSCCs from 3-d to 10-d (Fig. 2a1-a2, 4a1-a3), the degradation of $nC_{16}H_{34}$ following the free radical mechanism would result in generation of gases, PAHs and pyrobitumen along long-term deep burial (Tian et al., 2006).

4.1.2. Anhydrous $nC_{16}H_{34}$-minera systems

In the anhydrous $nC_{16}H_{34}$-mineral system, the unchanged surfaces of the quartz, feldspar and calcite grains suggest that the minerals without internal water (Supplementary data, Fig. S8a-c) experienced no alteration in the presence of hydrocarbons at 340 °C (Supplementary data, Fig. S6a1-c1), in consistent with the phenomena in previous study (Yuan et al., 2019b). The kaolinite and illite minerals that contained only structured water of hydroxyl (–OH) (Supplementary data, Fig. S8d, f) also did not experience obvious chemical alterations at 340 °C (Supplementary data, Fig. S6d1, f1), in consistent with the results of the series of heating experiments for investigating the phase transition of kaolinite and illite from low to high temperatures (100–1000 °C) (Yao and Gao, 2007; Wu et al., 2011). In contrast, the smectite with interlayer water (Supplementary Fig. S8e) experienced dehydration and illitization reactions during the heating processes, as evidenced by the texture changes (Supplementary Fig. S6e1), which is consistent with the results of some previous thermal experiments (Pan et al., 2010; Du et al., 2021a,b).

Free-radical thermal-cracking and cross-linking reactions occurred in all the anhydrous $nC_{16}H_{34}$-mineral systems, as indicated by the widely generation of nC_1-C_{15} alkanes, C_{17}-C_{30} alkanes, PAHs, pyrobitumen and H_2 (Fig. 1a, 2a2-g2, 3a2–a7) (Lewan, 1997; Yuan et al., 2019b). In addition to the free radical mechanism, the higher iC_4/nC_4 ratios (Supplementary data, Table S4) suggest an important role of the carbonium-ion mechanism in $nC_{16}H_{34}$ degradation in the anhydrous systems with clays. Similar to the anhydrous $nC_{16}H_{34}$ system, the absence of CO_2 (Fig. 1a) suggested no step oxidation nor decarboxylation reactions in the anhydrous systems with minerals, indicating that the oxygen in the different minerals (even the oxygen in water-containing clays) (Supplementary data, Fig. S8e) cannot oxidize the hydrocarbons at 340 °C in the present study, although smectite has been identified to oxidize some crude oil components at temperatures higher than 400 °C in previous studies (Pan et al., 2010). Involved as indirect reactants, the impact of minerals on the $nC_{16}H_{34}$ degradation in the anhydrous $nC_{16}H_{34}$-mineral systems should be attributed to the catalytic effect of chemical bonds in the different minerals (Supplementary data, Fig. S8) (Seewald, 2003).

In the $nC_{16}H_{34}$-quartz system, the generation of similar amount of C_1-C_5 gases (Fig. 1a; Fig. 2a2,-b2) and liquid C_6-C_{14} alkanes, but more HMW alkanes and PAHs with yellow to brown-yellow fluorescence colors (Fig. 3a1-a2; Fig. 4b1-b3), and the red-shift of the fluorescence spectra (Fig. 5a1-a3; Supplementary Table S5) (Bourdet et al., 2012; Bourdet et al., 2014) demonstrate that quartz promoted the free-radical cross-linking reaction significantly when compared to the I-a system without mineral, which was probably attribute to catalysis of the only Si–O bonds (Lewis acid sites) (Sun and Silverman, 1945) at the external surfaces of the quart grains experience no mineral alteration (Xu et al., 2011) (Supplementary data, Fig. S8a). Along long-term deep burial, the organic–inorganic interactions following such reaction pathways would result in generation of less LMW hydrocarbons, more HMW PAHs and pyrobitumen in the $nC_{16}H_{34}$-quartz system than in the anhydrous $nC_{16}H_{34}$ system (Fig. 9b).

In the anhydrous $nC_{16}H_{34}$-feldspar system, the generation of similar or slightly higher amount C_1-C_5 gases and liquid C_6-C_{14} alkanes (Fig. 1a, 2c2) but more HMW alkanes and PAHs with yellow to brown-yellow fluorescence color (Fig. 3a3, 4c1-c2), and the red-shift of the fluorescence spectra (Fig. 5a1–a3; Supplementary data, Table S5) (Bourdet et al., 2012, 2014; Liu et al., 2014) demonstrate that feldspar promoted the free-radical cross-linking reaction significantly when compared to the $nC_{16}H_{34}$ system without mineral. Similar to the quartz, the Si–O bonds at the external surfaces of the feldspar grains (Supplementary data, Fig. S8b) likely catalyzed the cross-linking reaction. The not less yields of gaseous hydrocarbons (Fig. 1a; Supplementary data, Table S4) and liquid C_6–C_{14} alkanes (Fig. 3a3) may be attributed to the Al–O bonds (Lewis acid sites) at the external surfaces of the feldspar grains (Supplementary Fig. S8b), which catalyzed the thermal-cracking to some extent (Corma et al., 1985; Kissin, 1996; Corma and Orchillés, 2000). Along long-term deep burial, the reaction pathways in the $nC_{16}H_{34}$-feldspar system would result in generation of less LMW hydrocarbons, more HMW PAHs and pyrobitumen than in the anhydrous $nC_{16}H_{34}$ system (Fig. 9c).

In the anhydrous $nC_{16}H_{34}$-calcite system, the generation of more gases (Fig. 1a, 2b4; Supplementary data, Table S4) and more HMW alkanes and PAHs with yellow fluorescence color (Fig. 3a4, 4d1–d4), and the red shift of the fluorescence spectra (Fig. 5a1–a3) demonstrate that calcite probably catalyzed both the free radical thermal-cracking and cross-linking reactions when compared to the $nC_{16}H_{34}$ system without mineral, consistent with the results of some previous studies (Eglinton et al., 1986; Xiao et al., 2010), though some studies suggest little or even inhibition impact of calcite on oil degradation (Pan et al., 2010; Hu et al., 2014). The catalysis was likely attributed to the presence of C–O bonds and Ca^{2+} at the external surfaces of the calcite grains (Supplementary data, Fig. S8c) (Ellig et al., 1985). Along long-term deep burial, the reaction pathways would result in generation of similar amounts of LMW hydrocarbons, HMW PAHs and pyrobitumen in the $nC_{16}H_{34}$-calcite system, but at a faster rate when compared to the anhydrous $nC_{16}H_{34}$ system (Fig. 9d).

In the anhydrous $nC_{16}H_{34}$-clay systems, the generation of more hydrocarbon gases and LMW alkanes (Fig. 1a; Supplementary data, Table S4), less PAHs but more M-BAHs with blue fluorescence color (Fig. 3a5-a7, 4e1-g3), the presence of pyrobitumen (Fig. 6b1-d2), and the blue shift of the fluorescence spectra of the liquid hydrocarbons (Fig. 5a1-a3) demonstrate that the clays (particularly smectite and kaolinite) promoted the thermal-cracking reaction significantly, and cross-linking reactions was altered to form more M-BAHs and pyrobitumen but much less PAHs. As proposed by previous studies (Corma et al., 1985; Corma and Orchillés, 2000; Bu et al., 2017), various B acid sites in the clay minerals (Supplementary data, Fig. S8d-f) probably catalyzed the $nC_{16}H_{34}$ cracking to form more LMW hydrocarbons and hydrogens (Fig. 1a; Supplementary data, Table S4) via the carbocation mechanism that initialed by catalytic attack of B acid sites on protons of C–C and C–H bonds. Smectite, which has large amount of B acid sites on both the external surfaces and in the interlayers (Supplementary data, Fig. S8e), exhibits the strongest promotion, followed by kaolinite with tetraherad-octahedral layer structure and with B acid sites relevant to exposed octahedral layer (Supplementary data, Fig. S8d), and illite with tetraherad-octahedral-tetraherad layer structure (Supplementary data, Fig. S8f). The L acid sites may also have some promotion impact on the thermal cracking, but much weaker compared to the B acid site (Corma et al., 1985; Kissin, 1996; Corma and Orchillés, 2000). Along long-term deep burial, these pathways in the $nC_{16}H_{34}$-clay systems would result in generation of more LMW hydrocarbons, less PAHs, and some pyrobitumen, and at a much faster rate when compared to the anhydrous $nC_{16}H_{34}$ system (Fig. 9e).

Overall, with organic–inorganic interactions following different pathways in the anhydrous systems with $nC_{16}H_{34}$ and different minerals in this study, smectite has the strongest promotion on generation of gaseous hydrocarbons, followed by kaolinite, illite, calcite, and feldspar, while quartz suppress the gaseous hydrocarbon generation in the anhydrous systems. Quartz, however, has the strongest promotion on generation of PAHs, followed by calcite and feldspar, and clay minerals likely suppressed the generation of PAHs.

4.2. Reaction pathways of organic–inorganic interactions in hydrous systems

4.2.1. Hydrous $nC_{16}H_{34}$-water system

High pressure has been verified to suppress oil cracking (Hill et al., 1996; Chen et al., 2014; Uguna et al., 2016). In the present study, the ambient pressure of the gold capsules was the same. Pressure in the hydrous FSCCs, though not monitored, should be higher than the anhydrous systems after generation of more gases. Thus, the higher yields of hydrocarbon gases and H_2, the higher C_1/C_2 and C_1/C_3 ratios in the hydrous gold capsules (Fig. 1; Supplementary data, Table S4), and the strong Raman signals of the gases in the hydrous FSCCs (Supplementary data, Fig. S2) suggest that both the D water and $CaCl_2$ water promoted the $C_{16}H_{34}$ degradation to generate more C_1-C_4 gaseous hydrocarbons (particular more methane) after heating for the same time. At the same time, both the D water and $CaCl_2$ water suppressed the generation of HMW alkanes and PAHs with yellow and brown fluorescence colors and also the generation of pyrobitumen, as evidenced by the blue and white-blue fluorescence colors (Supplementary data, Fig. S4-S5) and the blue-shift of the fluorescence spectra of the liquid hydrocarbons (Fig. 5), and the GC chromatograms of the liquid hydrocarbons (Fig. 3). These impacts were consistent with the results of thermal experiments conducted in Hastelloy reactors in our previous study (Yuan et al., 2019b), although some previous studies claimed that water suppresses (Price, 1993; Lewan, 1997; Uguna et al., 2016) or has little impact (Xie et al., 2016) on oil degradation processes. The promotion effect of water on generation of more LMW hydrocarbons (Fig. 1; Supplementary data, Table S4) and the inhibition effect on generation of HMW alkanes and PAHs (Figs. 3–6; Supplementary data, Figs. S4-S5) were probably the result of the additional hydrogen supply from the water (Lewan, 1997; Seewald, 2001, 2003; Yuan et al., 2019b), which accelerated the free-radical thermal-cracking reaction and suppressed the free-radical cross-linking reaction (Fig. 10a). Since the promotion and suppression effects of water on $nC_{16}H_{34}$ degradation were similar in both the gold capsules and the FSCCs, the absence of H_2 in the hydrous FSCCs (due to fast escape from the silica tube (Chou et al., 2008; Shang et al., 2009) indicated that the extra supply of hydrogen from water to the newly formed alkanes likely originated directly from hydrogen free radicals (Fig. 10a) (Lewan, 1997), but not the intermediate product of hydrogen gas (Seewald, 2001, 2003). In contrast to the anhydrous system, the presence of alcohols, organic acids (Fig. 7) and CO_2 (Fig. 1; Supplementary data, Fig. S3) in the hydrous systems suggest that the presence of water initiated the occurrence of step oxidation reactions of alkanes to form O-containing groups and the decarboxyla-

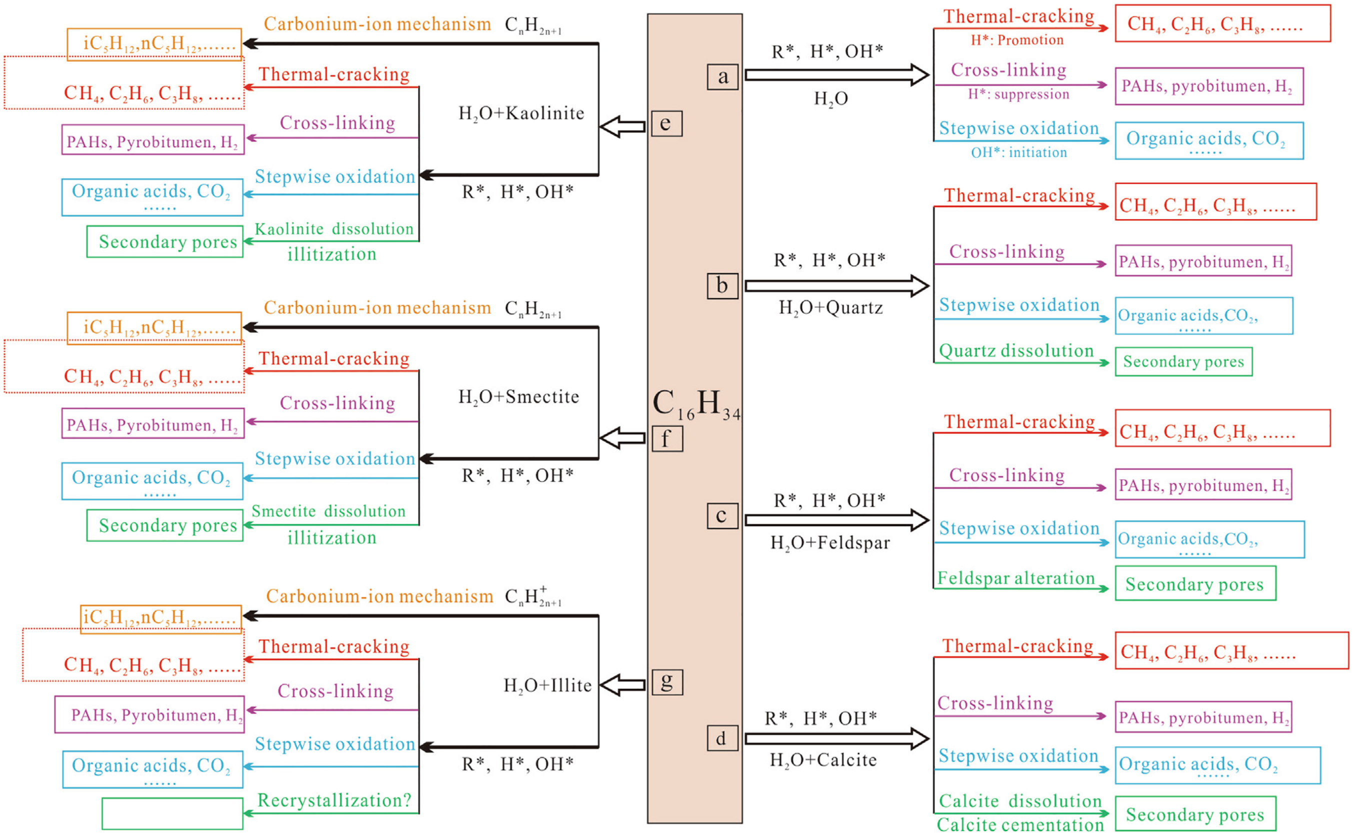

Fig. 10. Possible reaction pathways of organic–inorganic interactions and products in different $nC_{16}H_{34}$-D water–mineral systems.

tion reaction of organic acids to form CO_2 during the hydrocarbon degradation (Fig. 10a), as suggested by Seewald (2003) and Yuan et al. (2019b).

Comparisons show that the $CaCl_2$ water's promotion on the free-radical thermal-cracking reaction (Fig. 1c; Supplementary data, Fig. S2) and step-oxidation reactions (Fig. 7) and its suppression on free-radical cross-linking reaction (Figs. 3–5; Supplementary data, Figs. S4-S5) were weaker than that of the D water. The likely reason was that high Ca^{2+} concentration suppressed the formation of free radicals in water (Kuizenga et al., 1987). The less generation of H_2 in the $C_{16}H_{34}$-$CaCl_2$ water system than in the $C_{16}H_{34}$-distilled water system (Fig. 1b, c; Supplementary data, Table S4) also verified the less generation of hydrogen radical with the presence of high Ca^{2+} concentration. Noteworthy, the promotion or inhibition effects of the water on the hydrocarbon degradation always occurred, regardless of the presence or absence of minerals (Figs. 1–7; Supplementary data, Figs. S2–S5).

4.2.2. Hydrous $nC_{16}H_{34}$-water–mineral systems

In the presence of water (D water, $CaCl_2$ water), the SEM images and EDS analysis demonstrated various mineral alterations in the different $nC_{16}H_{34}$-water–mineral systems after heating for 3–10 d (Fig. 8; Supplementary data, Fig. S7). Similar to the hydrous systems without minerals, the water in the hydrous systems with minerals also promoted the free-radical thermal-cracking and step oxidation reactions and suppressed the cross-linking reaction, as evidenced by the higher yields of hydrocarbon gases (Fig. 1b, c; Supplementary data, Fig. S2), lower generation of PAHs (Fig. 3b2-b7, c2-c7), blue shift of the fluorescence spectra of the liquid hydrocarbons (Fig. 4; Supplementary data, Fig. S4), and the presence of O-containing species (Supplementary data, Fig. S3; Fig. 7). In addition, the generation of CO_2 and organic acids (Fig. 7) accompanying hydrocarbon degradation probably promoted the mineral alterations (Fig. 8; Supplementary data, Fig. S7) by providing more H^+ in the water solutions (Seewald, 2003; van Berk et al., 2013; Yuan et al., 2019b).

In the hydrous $nC_{16}H_{34}$-water–quartz systems, quartz dissolution was evident in both the systems with D water and $CaCl_2$ water (Fig. 8a,b), and additional calcite precipitation (Fig. 8c) occurred in the system with $CaCl_2$ water. The quartz dissolution occurred in acidic solutions (Crundwell, 2014), with the presence of organic acids and CO_2 generated following the step oxidation of $nC_{16}H_{34}$ (Figs. 1, 7). The secondary calcite in the system with $CaCl_2$ water was probably precipitated with combination of high concentration of Ca^{2+}, the consumption of H^+ and generation of HCO_3^- by quartz dissolution (Fig. 8c). In the $C_{16}H_{34}$-D water–quartz system, the generation of less C_1-C_3 gases (Fig. 1b), more C_7-C_{13} (Fig. 3b2), extremely less PAHs and blue shift of fluorescence spectra of the liquid hydrocarbons (Fig. 3b2 and 5b3), less CO_2 (Fig. 1b; Supplementary data, Table S4) and weaker Raman signal of oxygen-containing organics (Fig. 7a2) demonstrate that the presence of quartz suppressed both the free radical thermal-cracking (Fig. 1d2) and cross-linking reactions, and the step oxidation and decarboxylation reactions when compared to the hydrous system without mineral. The inhibition impact was likely attributed to the formation of Si-OH bonds (Brφnsted (B) acid) on the quartz surfaces and the aqueous H_4SiO_4 released in water during the quartz dissolution processes (Fig. 10b) (Du and de Leeuw, 2006; Crundwell, 2014). These reaction pathways in the $nC_{16}H_{34}$-water–quartz system result in generation of more LMW hydrocarbons and less PAHs and pyrobitumen in the long-term (Fig. 10b), but at a slower rate compared to the hydrous system without mineral. In the $nC_{16}H_{34}$-$CaCl_2$ water–quartz system, the inorganic mineral alteration reactions likely suppressed the free radical thermal-cracking reaction and the decarboxylation reaction, as supported by the relatively low yields of hydrocarbon gases and CO_2

(Fig. 1c; Supplementary data, Table S4, Fig. S2b1, b2), and the weaker Raman signal of oxygen-containing organics (Fig. 7b2). The slightly red-shift of the fluorescence spectra of the liquid hydrocarbons (Fig. 5c3) and gas chromatograms of the liquid hydrocarbons (Fig. 3c2) suggest weak promotion of the free radical cross-linking reaction. These reaction pathways would lead to generation of more HMW PAHs than in the III-a, II-a, and II-b systems; the generation of PAHs, however, should still be much lower than in the anhydrous systems.

In the $nC_{16}H_{34}$-D water-feldspar systems, the textures and compositions of the minerals identified (Fig. 8e,f) suggested that the mineral alteration reaction pathway in the presence of the generated organic acids and CO_2 (Fig. 1b, 7a3) was likely: feldspar dissolution → illite formation. This result is consistent with the pathways proposed in a previous study (Fu et al., 2009; Yuan et al., 2019b; Zhu and Lu, 2009). In the $nC_{16}H_{34}$-D water-feldspar system, the presence of feldspar promoted the free-radical thermal-cracking reaction, step oxidation reaction and decarboxylation reaction, and suppressed the cross-linking reactions, as evidenced by the generation of more hydrocarbon gases and CO_2 (Fig. 1b; Supplementary data, Fig. S2a3), more LMW hydrocarbons and less HMW alkanes and PAHs (Fig. 3b3) and blue shift of fluorescence spectra of the liquid hydrocarbons (Fig. 5b3) when compared to the hydrous system without mineral. As proposed by previous study (Yuan et al., 2019b), the mutual exchange of hydrogen and hydroxyl ions via the medium of water among minerals, water, and hydrocarbons probably promoted the free-radical thermal-cracking reaction (Fig. 2a4; Supplementary data, Fig. S3b, Table S4) and suppressed the cross-linking reactions (Supplementary data, Fig. S4b1-B3, 6b3). The promotion effect of mineral alteration on hydrocarbon degradation in the system with feldspar (II-a) evolved to be stronger in the 10-d experiment (Supplementary data, Fig. S2a3), which was likely due to the generation of clays in the system after 6-d heating (Fig. 8e, f). The Lewis acid sites in the feldspar and secondary illite (Supplementary data, Fig. S8b, f) promoted the decarboxylation reaction to form more CO_2 (Supplementary data, Table S4) (Bu et al., 2017; Yuan et al., 2019b). In the $nC_{16}H_{34}$-$CaCl_2$ water-feldspar systems, the mineral alteration pathway was likely: feldspar dissolution → illite formation → anorthite formation (Fig. 8g–i). Anorthite formation dominated after 6-d heating, in such a case, the direct replacement of K-feldspar by anorthite (Fig. 8i) led to weaker exchange of H^+ and OH^- between the minerals and hydrocarbons, which likely resulted in the weaker promotion on free-radical thermal-cracking reaction in the $CaCl_2$ water system than in the D water system. Overall, the reaction pathways in the hydrous system with feldspar likely led to generation of more LMW hydrocarbons and less PAHs over long-term geological time (Fig. 10c). In addition, secondary pores in feldspar grains would be produced.

In the hydrous $nC_{16}H_{34}$-water-calcite systems, the mineral alterations were very extensive in both the hydrous systems with D water and $CaCl_2$ water in the presence of generated organic acids and CO_2 (Fig. 1b,c, 7a4, b4). The mineral reaction pathway was likely: calcite dissolution → re-precipitation of euhedral calcite, and the calcite re-precipitation was more extensive in the system with $CaCl_2$ water than with D water (Fig. 8j–k). In the D water system with calcite, the presence of C-O and C-OH bonds formed during calcite dissolution (Pokrovsky et al., 2009; Xu et al., 2012) and adsorption of organics to the calcite surface with formation of polar compounds (Al-Busaidi et al., 2019; Marcano et al., 2019) probably led to further promotion of the free-radical thermal-cracking reaction and suppression of the cross-linking reaction, as evidenced by generation of more hydrocarbon gases (Fig. 1b, Supplementary data, Fig. S2a4), more LMW liquid hydrocarbons and less HMW alkanes and PAHs (Fig. 3b4) and blue shift of fluorescence spectra of the liquid hydrocarbons (Fig. 5b3) when compared to the hydrous system without mineral. The likely reason for the generation of more CO_2 (Fig. 1b; Supplementary data, Fig. S3a4) was that some calcite was dissolved by the organic acids formed during hydrocarbon degradation to release some CO_2 gas, as evidenced by the extensive leaching of calcite in the hydrous systems (Fig. 8J). Step oxidation and decarboxylation reactions also contributed some CO_2 (Seewald, 2003), as evidenced by the presence of the intermediate products including alcohols and organic acids (Fig. 7a4). In the $nC_{16}H_{34}$-$CaCl_2$ water-calcite system, the presence of calcite promoted the free-radical thermal-cracking reaction slightly to form more hydrocarbon gases (Fig. 1c) and LMW liquid hydrocarbons (Fig. 3c4), and promoted the free-radical cross-linking reaction extensively to form more HMW alkanes and PAHs (Fig. 3c4) when compared to the hydrous system without mineral. The precipitation of more secondary calcite (Fig. 8k) may result in the promotion of the free-radical cross-linking reaction, but the generation of HMW alkanes and PAHs is still smaller than in the anhydrous systems. (Fig. 3a4, c4 and 4d1–d3; Supplementary data, Fig. S5d1–d3). These reaction pathways likely result in the generation of more LMW hydrocarbons over long-term geological time (Fig. 10d). In addition, some secondary pores due to calcite dissolution are expected.

In the hydrous $nC_{16}H_{34}$-water-clay systems with kaolinite and smectite, dissolution and illitization of these clays were likely the most important mineral alteration reactions, particularly in the systems with $CaCl_2$ water, as indicated by the newly formed fibrous illite (Supplementary data, Fig. S7a-i). K^+ needed for illitization was likely originated from the impurity with potassium in the initial reactants (Supplementary data, Table S3). Without the formation of new minerals, recrystallization was likely the most important alteration reaction in the hydrous system with illite (Supplementary data, Fig. S7k-l). The $nC_{16}H_{34}$ degradation via carbonium-ion mechanism initiated by the B acid sites in the clays (Supplementary data, Fig. S8d-f) also occurred in the hydrous systems, but relative weaker considering the not big difference of the iC_4/nC_4 and iC_5/nC_5 ratios (Supplementary data, Table S4) in the system with and without clays, which is consistent with previous proposal that water suppresses catalytic effect of B acid sites on hydrocarbon cracking (Goldstein, 1983; Tannenbaum and Kaplan, 1985; Seewald, 2003). Similar to the $nC_{16}H_{34}$-D water-feldspar system, the mutual exchange of hydrogen and hydroxyl ions among the minerals, water, and hydrocarbons in the $nC_{16}H_{34}$-D water-clay systems probably led to further promotion of the free-radical thermal-cracking reaction to generate more hydrocarbon gases (Fig. 1b) and LMW liquid hydrocarbons (Fig. 3b5–b7), and suppression of the cross-linking reactions to generate less HMW alkanes, PAHs, and H_2 (Fig. 3b5–b7; Supplementary data, Table S4). The Lewis acid sites in the clays promoted the decarboxylation reaction to form more CO_2 (Supplementary data, Table S4, Fig. S3a5–a7) (Bu et al., 2017; Yuan et al., 2019b). In the $nC_{16}H_{34}$-$CaCl_2$ water-clay systems, the presence of clays promoted the free-radical thermal-cracking and cross-linking reactions and decarboxylation reaction to form more hydrocarbon gases, LMW liquid alkanes, CO_2 and HMW hydrocarbons, and less H_2 (Fig. 1c; Supplementary data, Figs. S3b5-b7 and 3c5-c7, Table S4). The blue shift of the fluorescence spectra of the liquid hydrocarbons (Fig. 5c1–c3; Supplementary data, Table S5) suggest that the promotion on thermal-cracking is stronger than on cross-linking. Hydrocarbon degradation via carbonium-ion mechanism also occurred weakly, as verified by the slightly higher iC_4/nC_4 and iC_5/nC_5 ratios (Supplementary data, Table S4). Overall, the reaction pathways in the hydrous systems with clay minerals led to generation of more LMW hydrocarbons at a much faster rate (Fig. 10e–g).

Overall, with different organic–inorganic interactions in the hydrous systems, the clay minerals have the strongest promotion on generation of LMW hydrocarbons, followed by calcite and feldspar, and the quartz slows down the generation of gaseous hydrocarbons. In the hydrous system with D water, the six types of minerals all suppressed the cross-linking reactions to form less HMW PAHs. In the hydrous system with $CaCl_2$ water, the clay minerals likely suppressed the cross-linking reactions to form less HMW PAHs, while quartz, calcite, and feldspar likely promoted the cross-linking reactions to form more HMW PAHs. Different minerals in deeply buried reservoirs can affect the alteration of each other (e.g., feldspar dissolution promotes illitization of smectite or kaolinite via releasing K^+ to the pore water, which in turn promotes more feldspar dissolution) (Glasmann, 1992; Yuan et al., 2019a), which probably will affect the evolution of hydrocarbons. From the results of this study, we can infer that combination of feldspar and semectite (kaolinite) probably lead to faster hydrocarbon degradation and generation of more LMW hydrocarbons; while combination of quartz and calcite may lead to generation of less HMW PAHs in the presence of water without high Ca^{2+} concentration. The impact of other complex mineral assemblages on hydrocarbon degradation, however, stills need further detailed studies.

4.3. Geological implications for deeply-buried hydrocarbon reservoirs

The different reaction pathways and products in the different $nC_{16}H_{34}$-water–mineral geochemical systems identified in the present study suggest that various organic–inorganic interactions that affected significantly by rock (mineral) types, oil/water saturations and water types (Zhao et al., 2007; Pan et al., 2010; Xiao et al., 2010; Yuan et al., 2019b) can occur extensively in deeply buried hydrocarbon reservoirs. Regardless of the rock types and mineral compositions, oil degradation in oil zone of reservoirs with little water is likely to generate more HMW PAHs and pyrobitumen, whereas oil degradation in oil–water transitional zone with a large amount of water is likely to generate more LMW gases and liquid hydrocarbons (Figs. 1–6; Supplementary data, Figs. S2–S5, Table S4) (Yuan et al., 2019b). At the same time, chemical diagenesis that controls reservoir quality evolution does not cease in the oil–water transitional zone at elevated temperatures (Fig. 8; Supplementary data, Fig. S7), as long as water is present (Molenaar et al., 2008; Yuan et al., 2018, 2019a,b). Continuous generation of secondary pores are expected in the oil–water transitional zone during deep burial processes, with leaching reactions induced by CO_2 and organic acids formed by stepwise oxidation of hydrocarbons (Seewald, 2003; van Berk et al., 2013; Yuan et al., 2019b). In addition, the extra supply of hydrogen from water to hydrocarbons and the simultaneous consumption of water during oil degradation at elevated temperatures (Seewald, 2003; Reeves et al., 2012; Yuan et al., 2019b) indicate that hydrocarbon reservoirs with low oil saturation after initial oil-charging may evolve to have higher hydrocarbon saturation when buried at deeper depth with higher temperatures.

Since water and minerals have considerably different impacts on oil degradation, hydrocarbon reservoirs that have the same hydrocarbon source but consist of different rocks (sandstones, mudstones, carbonate rocks) may have different hydrocarbon compositions after experiencing extensive organic–inorganic interactions during deep burial (Barker and Takach, 1992; Xu and Chou, 2017; Wang et al., 2018). This can result in complexity and difficulty in determining hydrocarbon-charge histories and hydrocarbon-source rock correlations of the deeply buried reservoirs. Fluorescence colors of hydrocarbons in pores and fluid inclusions of subsurface hydrocarbon reservoirs have been widely used to investigate hydrocarbon-charge periods (Bourdet et al., 2012, 2014; Liu et al., 2014; Cheng et al., 2019). The results in the present study, however, indicate that the same initial oil may evolve to different hydrocarbons with different fluorescence colors (Figs. 4 and 5; Supplementary data, Figs. S4, S5), even after experiencing the same burial-thermal history. As a result, in different zones (oil zone, oil–water transitional zone, water zone) of a hydrocarbon reservoir, except for the possibility of multi-charging of different hydrocarbons (Bourdet et al., 2012, 2014), hydrocarbons with different fluorescence colors may be formed via experiencing different organic–inorganic interactions due to the impact of different water saturation. Even in the same zone with similar oil/water saturation, hydrocarbons with different fluorescence colors may be present in pores and in fluid inclusions on small scales due to the impact of different minerals in the heterogeneous rocks. What's more, with the continuous occurrence of organic–inorganic interactions, changes in the chemical compositions of oil fluid inclusions and aqueous fluid inclusion with organics (e.g., acetic acid, wet gases) are very likely to occur during deep burial processes (Okubo, 2005; Ong et al., 2013; Ping et al., 2019), which will result in the adjustment of the homogenization temperature of the fluid inclusions. Thus, careful consideration is required when fluorescence colors and homogenization temperatures are employed to investigate the hydrocarbon-charge histories and hydrocarbon-source rock correlations of deeply buried hot hydrocarbon reservoirs (Okubo, 2005; Ong et al., 2013).

In addition, the inorganic parameters including rock types, water saturations and water types, also directly affect the kinetics of the organic–inorganic interactions in deeply buried reservoirs. The results of the present and previous experiments (Yuan et al., 2019b) suggested that NaCl water has the strongest promotion effect on hydrocarbon degradation, followed by distilled water and lastly $CaCl_2$ water, thus, oil reservoirs with high concentrations of Ca^{2+} in the formation water may preserve liquid hydrocarbons at deeper burial depths. When considering rock compositions, oil reservoirs with a high content of quartz may preserve liquid hydrocarbons to deeper depths than carbonate reservoirs or clastic reservoirs with large amount of aluminosilicate minerals (Zhao et al., 2007; George et al., 2008; Xu and Chou, 2017; Wang et al., 2018). Besides, liquid oils in reservoirs with low clay content may be preserved to a deeper depth than the same remnant liquid hydrocarbons in source rocks with high clay content. Thus, detailed quantitative investigations of the reaction kinetics in different hydrocarbon-water-rock (minerals) systems are warranted, which can improve the prediction of the quality evolution of charged hydrocarbons, porosity and secondary minerals in deeply buried reservoirs.

5. Conclusions

(i) Various organic–inorganic interactions following different reaction pathways occurred in the different hot $nC_{16}H_{34}$-(water)-(mineral) systems in the present study. Degradation of $nC_{16}H_{34}$ in anhydrous $nC_{16}H_{34}$ systems proceeds mainly through free radical mechanism, and the presence of D water and $CaCl_2$ water in hydrous $nC_{16}H_{34}$-water systems promoted the free-radical thermal-cracking reaction to generate more LMW liquid and gaseous hydrocarbons and suppress the free-radical cross-linking reaction to generate less HMW PAHs and pyrobitumen. In addition, water initiate the step oxidation and decarboxylation reactions to generation O-containing organics and CO_2, which may promote mineral alteration reactions. With introduction of hydrogen from water to hydrocarbons and formation of secondary pores by organic–inorganic interactions, reservoirs with low-medium hydrocarbon saturation after initial oil charging may have higher hydrocarbon saturation when buried at deep/ultra-deep depths.

(ii) Different minerals with different chemical bonds result in different influences on $C_{16}H_{34}$ degradation. In the anhydrous systems, smectite and kaolinite had the strongest promotion effect and generated the most gaseous hydrocarbons, followed by illite, calcite, and feldspar. Quartz suppressed the generation of gaseous hydrocarbons. Quartz, feldspar, and calcite promoted cross-linking reactions to generate more HMW PAHs and pyrobitumen. In contract, clays likely to generate more LMW PAHs and alkanes, as well as some pyrobitumen (particularly smectite). In the hydrous systems with D water, the quartz mineral likely retarded the generation of gaseous hydrocarbons, but feldspar, calcite, and clays probably promoted gas generation; all minerals suppressed the generation of HMW PAHs. In the hydrous systems with $CaCl_2$ water, the clays promoted the gas generation and retarded the generation of HMW PAHs. Feldspar and calcite promoted the generation of gases and HMW PAHs, whereas quartz suppressed the generation of gaseous hydrocarbons but promoted the generation of HMW PAHs.

(iii) Due to the different impact of waters and minerals on hydrocarbon degradation, reservoirs with little pore water (or with high Ca^{2+} concentration pore water) and reservoirs with high content of quartz are likely to preserve liquid hydrocarbons to deeper depths. Deeply buried reservoirs with similar burial-thermal history but high content of aluminosilicate minerals (particularly clays) and carbonate minerals are likely to develop nature gas reservoirs.

(iv) Different organic–inorganic reactions may result in considerable complexity of hydrocarbons in deeply buried hot reservoirs, which should be considered when fluorescence colors are employed to investigate hydrocarbon charge histories and hydrocarbon-source rock correlations in deeply buried layers.

Declaration of Competing Interest

The authors declare that they have no known competing financial interests or personal relationships that could have appeared to influence the work reported in this paper.

Acknowledgments

This study was funded by the Natural Science Foundation of China Project (Grant Nos. 41821002, 41872140), the Special fund for Taishan Scholar Project (Grant No.tsqn201909061), and the Fundamental Research Funds for the Central Universities (Grant No. 20CX06067A). Ms. Jianye Sun and Dr. Xiluo Hao at the Qingdao Institute of Marine Geology, China Geological Survey are thanked for their assistance in the Raman tests. Prof. Jinzhong Liu at the State Key Laboratory of Organic Geochemistry of the Guangzhou Institute of Geochemistry is thanked for the assistance in gold capsules heating and testing. We sincerely thank the GSF Associate Editor Dr. Vinod Samuel and another two anonymous reviewers for reviewing our work and for their great advices and constructive comments.

Appendix A. Supplementary data

Supplementary data to this article can be found online at https://doi.org/10.1016/j.gsf.2021.101322.

References

Al-Busaidi, I.K., Al-Maamari, R.S., Karimi, M., Naser, J., 2019. Effect of different polar organic compounds on wettability of calcite surfaces. J. Petrol. Sci. Eng. 180, 569–583.

Barker, C., Takach, N.E., 1992. Prediction of Natural Gas Composition in Ultradeep Sandstone Reservoirs. AAPG Bull. 76, 1859–1873.

Bjørlykke, K., 2014. Relationships between depositional environments, burial history and rock properties. Some principal aspects of diagenetic process in sedimentary basins. Sediment. Geol. 301, 1–14.

Bourdet, J., Eadington, P., Volk, H., George, S.C., Pironon, J., Kempton, R., 2012. Chemical changes of fluid inclusion oil trapped during the evolution of an oil reservoir: Jabiru-1A case study (Timor Sea, Australia). Mar. Petrol. Geol 36 (1), 118–139.

Bourdet, J., Burruss, R.C., Chou, I.-M., Kempton, R., Liu, K., Hung, N.V., 2014. Evidence for a palaeo-oil column and alteration of residual oil in a gas-condensate field: Integrated oil inclusion and experimental results. Geochim. Cosmochim. Acta 142, 362–385.

Bu, H., Yuan, P., Liu, H., Liu, D., Liu, J., He, H., Zhou, J., Song, H., Li, Z., 2017. Effects of complexation between organic matter (OM) and clay mineral on OM pyrolysis. Geochim. Cosmochim. Acta 212, 1–15.

Caumon, M.-C., Robert, P., Laverret, E., Tarantola, A., Randi, A., Pironon, J., Dubessy, J., Girard, J.-P., 2014. Determination of methane content in NaCl–H_2O fluid inclusions by Raman spectroscopy. Calibration and application to the external part of the Central Alps (Switzerland). Chem. Geol. 378-379, 52–61.

Chen, Z.H, Ma, Z.J., Zha, M., Sha, X., Zhang, S.C., Bao, Y.S., 2014. The effects of high pressure on oil-to-gas cracking during laboratory simulation experiments. J. Petrol. Geol. 37 (2), 143–162.

Cheng, P., Tian, H., Xiao, X., Liu, D., Zhang, Y., Huang, B., Zhou, Q., Gai, H., Li, T., 2019. Fluorescence lifetimes of crude oils and oil inclusions: A preliminary study in the Western Pearl River Mouth Basin, South China Sea. Org. Geochem. 134, 16–31.

Chou, I.-M., Wang, A., 2017. Application of laser Raman micro-analyses to Earth and planetary materials. J. Asian Earth Sci. 145, 309–333.

Chou, I.-M., Song, Y., Burruss, R.C., 2008. A new method for synthesizing fluid inclusions in fused silica capillaries containing organic and inorganic material. Geochim. Cosmochim. Acta. 72 (21), 5217–5231.

Corma, A., Orchillés, A.V., 2000. Current views on the mechanism of catalytic cracking. Micropor. Mesopor. Mat. 35-36, 21–30.

Corma, A., Planelles, J., Sánchez-Marín, J., Tomás, F., 1985. The role of different types of acid site in the cracking of alkanes on zeolite catalysts. J. Catal. 93, 30–37.

Crundwell, F.K., 2014. The mechanism of dissolution of minerals in acidic and alkaline solutions: Part II Application of a new theory to silicates, aluminosilicates and quartz. Hydrometallurgy 149, 265–275.

Du, J.Z., Cai, J.G., Chao, Q., Song, M.S., Wang, X.J., 2021a. Variations and geological significance of solid acidity during smectite illitization. Appl. Clay Sci. 204, 1–11.

Du, J., Cai, J., Lei, T., Li, Y., 2021b. Diversified roles of mineral transformation in controllinghydrocarbon generation process, mechanism, and pattern. Geosci. Front. 12 (2), 725–736.

Du, Z., de Leeuw, N.H., 2006. Molecular dynamics simulations of hydration, dissolution and nucleation processes at the α-quartz (0001) surface in liquid water. Dalton Trans., 2623–2634

Eglinton, T.I., Rowland, S.J., Curtis, C.D., Douglas, A.G., 1986. Kerogen-mineral reactions at raised temperatures in the presence of water. Org. Geochem. 10 (4-6), 1041–1052.

Ellig, D.L., Lai, C.K., Mead, D.W., Longwell, J.P., Peters, W.A., 1985. Pyrolysis of volatile aromatic hydrocarbons and n-heptane over calcium oxide and quartz. Ind. Eng. Chem. Process Des. Dev. 24 (4), 1080–1087.

Fu, Q.i., Lu, P., Konishi, H., Dilmore, R., Xu, H., Seyfried, W.E., Zhu, C., 2009. Coupled alkali-feldspar dissolution and secondary mineral precipitation in batch systems: 1. New experiments at 200 °C and 300 bars. Chem. Geol. 258 (3-4), 125–135.

George, S.C., Volk, H., Dutkiewicz, A., Ridley, J., Buick, R., 2008. Preservation of hydrocarbons and biomarkers in oil trapped inside fluid inclusions for >2 billion years. Geochim. Cosmochim. Acta 72, 844–870.

Girard, J.-P., Munz, I.A., Johansen, H., Lacharpagne, J.-C., Sommer, F., 2002. Diagenesis of the hild brent sandstones, northern north sea: isotopic evidence for the prevailing influence of deep basinal water. J. Sediment. Res. 72 (6), 746–759.

Glasmann, J.R., 1992. The fate of feldspar in Brent Group reservoirs, North Sea: A regional synthesis of diagenesis in shallow, intermediate, and deep burial environments. Geological Society, London, Special Publications 61 (1), 329–350.

Goldstein, T.P., 1983. Geocatalytic reactions in formation and maturation of petroleum. AAPGBull 67, 152–159.

Haas, J. L., 1976. Physical properties of the coexisting phases and thermochemical properties of the H_2O component in boiling NaCl solutions. USGS Bull. 1421.

Helgeson, H.C., Knox, A.M., Owens, C.E., Shock, E.L., 1993. Petroleum, oil field waters, and authigenic mineral assemblages Are they in metastable equilibrium in hydrocarbon reservoirs. Geochim. Cosmochim. Acta 57 (14), 3295–3339.

Higgs, K.E., Funnell, R.H., Reyes, A.G., 2013. Changes in reservoir heterogeneity and quality as a response to high partial pressures of CO_2 in a gas reservoir, New Zealand. Mar. Petrol. Geol. 48, 293–322.

Higgs, K.E., Zwingmann, H., Reyes, A.G., Funnell, R.H., 2007. Diagenesis, Porosity Evolution, and Petroleum Emplacement in Tight Gas Reservoirs, Taranaki Basin, New Zealand. J. Sediment. Res. 77 (12), 1003–1025.

Hill, R.J., Tang, Y., Kaplan, I.R., 2003. Insights into oil cracking based on laboratory experiments. O. Geochem. 34 (12), 1651–1672.

Hill, R.J., Tang, Y., Kaplan, I.R., Jenden, P.D., 1996. The Influence of Pressure on the Thermal Cracking of Oil. Energ. Fuel 10 (4), 873–882.

Hoering, T.C., 1984. Thermal reactions of kerogen with added water, heavy water and pure organic substances. Org. Geochem. 5 (4), 267–278.

Hu, M., Cheng, Z., Zhang, M., Liu, M., Song, L., Zhang, Y., Li, J., 2014. Effect of Calcite, Kaolinite, Gypsum, and Montmorillonite on Huadian Oil Shale Kerogen Pyrolysis. Energ. Fuel. 28 (3), 1860–1867.

Kissin, Y.V., 1996. Chemical Mechanism of Hydrocarbon Cracking over Solid Acidic Catalysts. J. Catal. 163 (1), 50–62.

Kuizenga, A., van Haeringen, N.J., Kijlstra, A., 1987. Inhibition of hydroxyl radical formation by human tears. Invest. Ophthalmol. Vis. Sci. 28, 305–313.

Lai, J., Wang, G., Chai, Y.u., Xin, Y.i., Wu, Q., Zhang, X., Sun, Y., 2017. Deep burial diagenesis and reservoir quality evolution of high-temperature, high-pressure sandstones: Examples from Lower Cretaceous Bashijiqike Formation in Keshen area, Kuqa depression. Tarim basin of China. AAPG Bull. 101 (06), 829–862.

Lewan, M.D., 1997. Experiments on the role of water in petroleum formation. Geochim. Cosmochim. Acta 61 (17), 3691–3723.

Li, F., Cao, Y., Li, W., Zhang, L., 2018. CO_2 mineral trapping: Hydrothermal experimental assessments on the thermodynamic stability of dawsonite at 4.3 Mpa pCO_2 and elevated temperatures. Greenh. Gases 8 (1), 77–92.

Li, F., Li, W., Yu, Z., Liu, N.a., Yang, H., Liu, L.i., 2017. Dawsonite occurrences related to the age and origin of CO_2 influx in sandstone reservoirs: A case study in the Songliao Basin, NE China. Geochem. Geophy. Geosy. 18 (1), 346–368.

Liu, K., George, S.C., Lu, X., Gong, S.e., Tian, H., Gui, L., 2014. Innovative fluorescence spectroscopic techniques for rapidly characterising oil inclusions. Org. Geochem. 72, 34–45.

Liu, Q., Zhu, D., Meng, Q., Liu, J., Wu, X., Zhou, B., Fu, Q.i., Jin, Z., 2019. The scientific connotation of oil and gas formations under deep fluids and organic-inorganic interaction. Sci. China Earth Sci. 62 (3), 507–528.

Macquaker, J.H.S., Taylor, K.G., Keller, M., Polya, D., 2014. Compositional controls on early diagenetic pathways in fine-grained sedimentary rocks: Implications for predicting unconventional reservoir attributes of mudstones. AAPGBull. 98 (3), 587–603.

Magnotti, G., KC, U., Varghese, P.L., Barlow, R.S., 2015. Raman spectra of methane, ethylene, ethane, dimethyl ether, formaldehyde and propane for combustion applications. J. Quant Spectrosc. Ra. 163, 80–101.

Marcano, M.C., Kim, S., Taylor, S.D., Becker, U., 2019. Exploring wettability by imaging the adsorption of crude oil, re-dissolved asphaltene, and phenol solutions onto calcite. Implications to sorption mechanisms and molecular structure of surface-active compounds in crude oil. Chem. Geol. 525, 462–478.

Molenaar, N., Cyziene, J., Sliaupa, S., Craven, J., 2008. Lack of inhibiting effect of oil emplacement on quartz cementation: Evidence from Cambrian reservoir sandstones, Paleozoic Baltic Basin. Geol. Soc. Am. Bull. 120 (9-10), 1280–1295.

Molenaar, N., Felder, M., Bär, K., Götz, A.E., 2015. What classic greywacke (litharenite) can reveal about feldspar diagenesis: An example from Permian Rotliegend sandstone in Hessen, Germany. Sediment Geol 326, 79–93.

Mu, N., Fu, Y., Schulz, H.-M., van Berk, W., 2016. Authigenic albite formation due to water–rock interactions — Case study: Magnus oilfield (UK, Northern North Sea). Sediment. Geol. 331, 30–41.

Okubo, S., 2005. Effects of thermal cracking of hydrocarbons on the homogenization temperature of fluid inclusions from the Niigata oil and gas fields. Japan. Appl. Geochem. 20 (2), 255–260.

Ong, A., Pironon, J., Robert, P., Dubessy, J., Caumon, M.-C., Randi, A., Chailan, O., Girard, J.-P., 2013. In situ decarboxylation of acetic and formic acids in aqueous inclusions as a possible way to produce excess CH_4. Geofluids 13 (3), 298–304.

Palandri, J.L., Kharaka, Y.K., 2004. A Compilation of RateParameters of Water-Mineral Interaction Kinetics for Application to Geochemical Modeling. USGS, Menlo Park, CA.

Pan, C., Geng, A., Zhong, N., Liu, J., Yu, L., 2009. Kerogen pyrolysis in the presence and absence of water and minerals: Amounts and compositions of bitumen and liquid hydrocarbons. Fuel 88 (5), 909–919.

Pan, C., Jiang, L., Liu, J., Zhang, S., Zhu, G., 2010. The effects of calcite and montmorillonite on oil cracking in confined pyrolysis experiments. Org. Geochem. 41 (7), 611–626.

Pang, X., Jia, C., Zhang, K., Li, M., Wang, Y., Peng, J., Li, B., Chen, J., 2020. The dead line for oil and gas and implication for fossil resource prediction. Earth Syst. Sci. Data 12 (1), 577–590.

Ping, H., Chen, H., George, S.C., Li, C., Hu, S., 2019. Relationship between the fluorescence colour of oil inclusions and thermal maturity in the Dongying Depression, Bohai Bay Basin, China: Part 2. fluorescence evolution of oil in the context of petroleum generation, expulsion and cracking under geological conditions. Mar. Petrol. Geol 103, 306–319.

Pokrovsky, O.S., Golubev, S.V., Schott, J., Castillo, A., 2009. Calcite, dolomite and magnesite dissolution kinetics in aqueous solutions at acid to circumneutral pH, 25 to 150 °C and 1 to 55 atm pCO_2: New constraints on CO_2 sequestration in sedimentary basins. Chem. Geol 265, 26–32.

Price, L.C., 1993. Thermal stability of hydrocarbons in nature: Limits, evidence, characteristics, and possible controls. Geochim. Cosmochim. Acta 57 (14), 3261–3280.

Reeves, E.P., Seewald, J.S., Sylva, S.P., 2012. Hydrogen isotope exchange between *n*-alkanes and water under hydrothermal conditions. Geochim. Cosmochim. Acta 77, 582–599.

Seewald, J.S., 2001. Aqueous geochemistry of low molecular weight hydrocarbons at elevated temperatures and pressures: constraints from mineral buffered laboratory experiments. Geochim. Cosmochim. Acta 65 (10), 1641–1664.

Seewald, J.S., 2003. Organic-inorganic interactions in petroleum-producing sedimentary basins. Nature 426 (6964), 327–333.

Shang, L., Chou, I.-M., Lu, W., Burruss, R.C., Zhang, Y., 2009. Determination of diffusion coefficients of hydrogen in fused silica between 296 and 523K by Raman spectroscopy and application of fused silica capillaries in studying redox reactions. Geochim. Cosmochim. Acta 73 (18), 5435–5443.

Siskin, M., Katritzky, A.R., 1991. Reactivity of organic compounds in hot water: geochemical and technological implications. Science 254 (5029), 231–237.

Stasiuk, L.D., Snowdon, L.R., 1997. Fluorescence micro-spectrometry of synthetic and natural hydrocarbon fluid inclusions: crude oil chemistry, density and application to petroleum migration. Appl. Geochem. 12 (3), 229–241.

Surdam, R.C., Crossey, L.J., 1987. Integrated diagenetic modeling: a process-oriented approach for clastic systems. Annu. Rev. Earth Pl. Sc. 15 (1), 141–170.

Sun, K.-H., Silverman, A., 1945. Lewis acid-base theory applied to glass. J. Am. Ceram. Soc. 28 (1), 8–11.

Tannenbaum, E., Kaplan, I.R., 1985. Hydrocarbons generated during hydrous and dry pyrolysis of. Nature 317, 708–709.

Tian, H., Wang, Z., Xiao, Z., Li, X., Xiao, X., 2006. Oil cracking to gases: Kinetic modeling and geological significance. Chinese Sci. Bull. 51 (22), 2763–2770.

Tian, H., Xiao, X., Wilkins, R.W.T., Gan, H., Guo, L., Yang, L., 2010. Genetic origins of marine gases in the Tazhong area of the Tarim basin, NW China: Implications from the pyrolysis of marine kerogens and crude oil. Int. J. Coal. Geol. 82 (1-2), 17–26.

Tutolo, B.M., Luhmann, A.J., Kong, X.-Z., Saar, M.O., Seyfried, W.E., 2015. CO_2 sequestration in feldspar-rich sandstone: Coupled evolution of fluid chemistry, mineral reaction rates, and hydrogeochemical properties. Geochim. Cosmochim. Acta 160, 132–154.

Uguna, C.N., Carr, A.D., Snape, C.E., Meredith, W., 2016. Retardation of oil cracking to gas and pressure induced combination reactions to account for viscous oil in deep petroleum basins: evidence from oil and *n*-hexadecane pyrolysis at water pressures up to 900 bar. Org. Geochem. 97, 61–73.

van Berk, W., Fu, Y., Schulz, H.-M., 2015. Creation of pre-oil-charging porosity by migration of source-rock-derived corrosive fluids through carbonate reservoirs: one-dimensional reactive mass transport modelling. Petrol. Geosci. 21 (1), 35–42.

van Berk, W., Schulz, H.-M., Fu, Y., 2013. Controls on CO_2 fate and behavior in the Gullfaks oil field (Norway): How hydrogeochemical modeling can help decipher organic-inorganic interactions. AAPG Bull. 97 (12), 2233–2255.

Wan, Y., Bourdet, J., Hu, W., Kang, X., Heath, C., Qiu, Y., Gao, W., Wang, X., 2021. Experimental investigations on the thermochemical oxidation of *n*-alkane and alcohol compounds by MnO_2 and Fe_2O_3 at temperatures up to 325 °C. Chem. Geol. 559, 119982.

Wang, X., Song, Y., Chou, I.M., Qiu, Y., 2018. Raman spectroscopic characterization of cracking and hydrolysis of *n*-pentane and *n*-octadecane at 300–375℃ with geological implications. Energ. Explor. Exploit. 36 (4), 955–970.

Wang, X., Wan, Y., Hu, W., Chou, I.-M., Cao, J., Wang, X., Wang, M., Li, Z., 2016. In situ observations of liquid–liquid phase separation in aqueous $ZnSO_4$ solutions at temperatures up to 400 °C: Implications for Zn^{2+}-SO_4^{2-} association and evolution of submarine hydrothermal fluids. Geochim. Cosmochim. Acta 181, 126–143.

Wang, Z.J., Lu, M.H., Zhou, X.F., Wang, T.Y., 2013. Raman spectroscopy detection of the trace ethylene gas. J. Changzi Univ. 30, 21–24.

Waples, D.W., 2000. The kinetics of in-reservoir oil destruction and gas formation: constraints from experimental and empirical data, and from thermodynamics. Org. Geochem. 31 (6), 553–575.

Wei, L., Gao, Z., Mastalerz, M., Schimmelmann, A., Gao, L., Wang, X., Liu, X., Wang, Y., Qiu, Z., 2019. Influence of water hydrogen on the hydrogen stable isotope ratio of methane at low versus high temperatures of methanogenesis. Org Geochem 128, 137–147.

Worden, R.H., Bukar, M., Shell, P., 2018. The effect of oil emplacement on quartz cementation in a deeply buried sandstone reservoir. AAPG Bull. 102 (01), 49–75.

Worden, R.H., Oxtoby, N.H., Smalley, P.C., 1998. Can oil emplacement prevent quartz cementation in sandstones? Petrol. Geosci. 4 (2), 129–137.

Wu, H., Yu, J., Gao, J., Lei, X., 2011. Phase transition of ammonium illite at high temperature. J. Chin. Ceram. Soc. 39, 635–640.

Xiao, Q.L., Sun, Y., Zhang, Y., 2010. The role of reservoir mediums in natural oil cracking: Preliminary experimental results in a confined system. Chinese. Sci. Bull. 55 (33), 3787–3793.

Xie, L., Sun, Y., Uguna, C.N., Li, Y., Snape, C.E., Meredith, W., 2016. Thermal Cracking of Oil under Water Pressure up to 900 bar at High Thermal Maturities. 1. Gas Compositions and Carbon Isotopes. Energ. Fuel. 30 (4), 2617–2627.

Xu, H., Hou, D., Löhr, S.C., Liu, Q., George, S.C., 2020. Early diagenetic pyrite cementation influences molecular composition of sedimentary organic matter in the Dongying Depression. China. Ore. Geochem. 144, 104019. https://doi.org/10.1016/j.orggeochem.2020.104019.

Xu, H., Liu, Q., Zhu, D., Meng, Q., Jin, Z., Fu, Q.i., George, S.C., 2021. Hydrothermal catalytic conversion and metastable equilibrium of organic compounds in the Jinding Zn/Pb ore deposit. Geochim. Cosmochim. Acta 307, 133–150.

Xu, J., Fan, C., Teng, H.H., 2012. Calcite dissolution kinetics in view of Gibbs free energy, dislocation density, and pCO_2. Chem. Geol. 322-323, 11–18.

Xu, J.P, Chen, J.D, Cheng, M.L., 2011. Cross-linking and grafting with PS of EPDM in the presence of Lewis acids. J. Appl. Polym. Sci. 119 (5), 2961–2967.

Xu, X., Chou, I.-M., 2017. Raman spectroscopic study of cracking and hydrolysis of propane in fused silica capillary capsules between 300 and 400 °C. J. Raman. Spectrosc. 48 (11), 1420–1425.

Yao, L., Gao, Z., 2007. A study on the thermal transformation of Suzhou Kaolinite. Acta. Miner. Sin., 255–261

Yuan, G., Cao, Y., Gluyas, J., Cao, X.u., Zhang, W., 2018. Petrography, fluid-inclusion, isotope, and trace-element constraints on the origin of quartz cementation and feldspar dissolution and the associated fluid evolution in arkosic sandstones. AAPG Bull. 102 (05), 761–792.

Yuan, G., Cao, Y., Gluyas, J., Li, X., Xi, K., Wang, Y., Jia, Z., Sun, P., Oxtoby, N.H., 2015. Feldspar dissolution, authigenic clays, and quartz cements in open and closed sandstone geochemical systems during diagenesis: Typical examples from two sags in Bohai Bay Basin, East China. AAPG Bull. 99 (11), 2121–2154.

Yuan, G., Cao, Y., Schulz, H.-M., Hao, F., Gluyas, J., Liu, K., Yang, T., Wang, Y., Xi, K., Li, F., 2019a. A review of feldspar alteration and its geological significance in sedimentary basins: From shallow aquifers to deep hydrocarbon reservoirs. Earth-Sci. Rev. 191, 114–140.

Yuan, G., Cao, Y., Zan, N., Schulz, H.-M., Gluyas, J., Hao, F., Jin, Q., Liu, K., Wang, Y., Chen, Z., Jia, Z., 2019b. Coupled mineral alteration and oil degradation in thermal oil-water-feldspar systems and implications for organic-inorganic interactions in hydrocarbon reservoirs. Geochim. Cosmochim. Acta 248, 61–87.

Zhang, T., Amrani, A., Ellis, G.S., Ma, Q., Tang, Y., 2008a. Experimental investigation on thermochemical sulfate reduction by H2S initiation. Geochim. Cosmochim. Acta 72 (14), 3518–3530.

Zhang, T., Ellis, G.S., Walters, C.C., Kelemen, S.R., Wang, K.-S., Tang, Y., 2008b. Geochemical signatures of thermochemical sulfate reduction in controlled hydrous pyrolysis experiments. Org. Geochem. 39 (3), 308–328.

Zhao, L.B., Zhang, T.H., Yang, X.J., Guo, X.B., Rao, W.H., 2018. Gas-water distribution characteristics and formation mechanics in deep tight sandstone gas reservoirs of Keshen block, Kuqa Depression. Tarim Basin. Nat. Gas Geosci. 29, 500–509.

Zhao, W.Z., Wang, Z.Y., Zhang, S.C., Wang, H.J., 2007. Gas generation conditions of crude oil cracking in different geological environments. Sci. China Earth Sci. 37, 63–68.

Zhu, C., Lu, P., 2009. Alkali feldspar dissolution and secondary mineral precipitation in batch systems: 3. Saturation states of product minerals and reaction paths. Geochim. Cosmochim. Acta 73 (11), 3171–3200.

Zou, C.N., Yang, Z., Tao, S.Z., Yuan, X.J., Zhu, R.K., Hou, L.H., Wu, S.T., Sun, L., Zhang, G. S., Bai, B., Wang, L., Gao, X.H., Pang, Z.L., 2013. Continuous hydrocarbon accumulation over a large area as a distinguishing characteristic of unconventional petroleum: The Ordos Basin, North-Central China. Earth-Sci Rev 126, 358–369.

Zou, X.Y., Lv, X., He, M.C., 2007. Quantative analytsis of common acid radical ions by laser Raman spectrometry. Rock Miner. Anal. 26, 26–28.